Analysis, Design and Manufacture of a Solarised Gas Turbine Compressor

by

Timmo Marc Schommarz

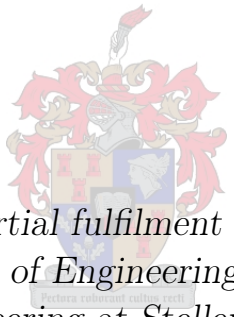

Thesis presented in partial fulfilment of the requirements for the degree of Master of Engineering (Mechanical) in the Faculty of Engineering at Stellenbosch University

Supervisor: Prof. T.W. Von Backström
Co-supervisor: Prof. S.J. Van Der Spuy

April 2019

The financial assistance of the National Research Foundation (NRF) towards this research is hereby acknowledged. Opinions expressed and conclusions arrived at, are those of the author and are not necessarily to be attributed to the NRF.

Declaration

By submitting this thesis electronically, I declare that the entirety of the work contained therein is my own, original work, that I am the sole author thereof (save to the extent explicitly otherwise stated), that reproduction and publication thereof by Stellenbosch University will not infringe any third party rights and that I have not previously in its entirety or in part submitted it for obtaining any qualification.

Date: April 2019

Plagiarism Declaration

1. Plagiarism is the use of ideas, material and other intellectual property of another's work and to present it as my own.
2. I agree that plagiarism is a punishable offence because it constitutes theft.
3. I also understand that direct translations are plagiarism.
4. Accordingly all quotations and contributions from any source whatsoever (including the internet) have been cited fully. I understand that the reproduction of text without quotation marks (even when the source is cited) is plagiarism.
5. I declare that the work contained in this assignment, except where otherwise stated, is my original work and that I have not previously (in its entirety or in part) submitted it for grading in this module/assignment or another module/assignment.

Student number	Signature
Initials and surname	Date

Abstract

Analysis, Design and Manufacture of a Solarised Gas Turbine Compressor

T.M. Schommarz

Department of Mechanical and Mechatronic Engineering,
University of Stellenbosch,
Private Bag X1, Matieland 7602, South Africa.

Thesis: MEng (Mech)

April 2019

An existing three-dimensional fluid mechanical design of a compressor is reviewed and compared to mean-line simulation results obtained using the CompAero® compressor design code. Mean-line simulation results give a compressor total-to-static pressure ratio of 3.2. The three-dimensional CFD analysis performed using ANSYS CFX® calculates a total-to-static pressure ratio of 3.4. This is an increase of 31% from the pressure ratio of the currently installed compressor (2.6). ANSYS Mechanical® is used to perform finite element analyses for deformation, stress and vibrational behaviour. The maximum calculated axial deflection is 0.24 mm. The calculated maximum equivalent stress is 218 MPa. All vibration modes occur at frequencies higher than the operating speed of the compressor. The first damped frequency occurs at 837 Hz which represents and over-speed condition of 9.24%. Over-speed simulations to 110% operating speed calculate a maximum stress in the impeller of 264 MPa. This is 1.8 times less than the yield strength of Aluminium 7075 which was used to manufacture the part. Axial forces due to the increased outlet pressure of the compressor are calculated. The total load on the angular contact bearing increased from 376 N, as experienced with the old compressor, to 955 N when using the new compressor. The new impeller and diffuser are designed using the Autodesk Inventor® CAD program. The components are machined using five- and three-axis computer-aided milling.

Uittreksel

Analise, Ontwerp en Vervadiging van 'n Gasturbine Kompressor vir Sontermiese Toepassing

("Analysis, Design and Manufacture of a Solarised Gas Turbine Compressor")

T.M. Schommarz

Departement Meganiese en Megatroniese Ingenieurswese,
Universiteit van Stellenbosch,
Privaatsak X1, Matieland 7602, Suid Afrika.

Tesis: MIng (Meg)

April 2019

'n Vorige drie-dimensionele, vloei-meganiese ontwerp word hersien en met een-dimensionele berekeninge vergelyk. Een-dimensionele berekeninge is met die CompAero® sagteware pakket gedoen en voorspel 'n totaal-tot-statiese druk-verhouding van 3.2. Die drie-dimensionele berekenig is met ANSYS CFX® gedoen en voorspel 'n totaal-tot-statiese drukverhouding van 3.4. Die druk-verhouding word met 31% verbeter vanaf die van die kompressor wat huidiglik gebruik word (2.6). ANSYS Mechanical® is gebruik om strukturele analises vir vervorming, spanning en vibrasie uit te voer. Die grootste aksiale vervorming is 0.24 mm. Die grootste spanning word bereken as 218 MPa. Alle modes van vibrasie is hoër as die ontwerpspoed van die kompressorrotor. Die eer-ste gedempte mode verskyn by 837 Hz wat gelyk is aan 'n oor-spoed toestand van 9.24%. Oor-spoed berekeninge tot en met 110% ontwerpsspoed bereken 'n maksimum spanning van 264 MPa. Hierdie spanning is 1.8 keer kleiner as die swik-krag van Aluminium 7075. Die totale las op die aksiale laër verhoog van 376 N, soos bereken met die ou kompressor, na 955 N as gevolg van die styging in druk. Die nuwe rotor and stator is in Autodesk Inventor® ontwerp en vervardig met vyf- en drie-as rekenaar-ondersteunde masjienering.

Acknowledgements

I would like to thank Professor von Backström for his technical guidance throughout this project, for the funding provided and the many gas turbine stories shared.

Professor van der Spuy I would like to thank for always being the voice of reason during this journey. Thank you also for the many insightful and inspiring comments.

Many thanks also to Hoosen Akram and Paul Keenley for sharing their knowledge regarding Non-Destructive Testing.

Mister Ferdi Zietsman and the staff of the Mechanical and Mechatronic workshop are thanked for their timely help and plentiful kindness.

A heart-felt thank you to Mister Chad Swart and the staff of the Stellenbosch Technology Centre. This compressor would never have seen the light of day without you.

Lastly to Clarice, Daniel, Marco and David – thank you friends.

Dedications

Gewidmet meinem Vater.

Contents

List of Figures

List of Tables

Nomenclature

Abbreviations

CAD Computer-Aided Design

CAM Computer-Aided Manufacturing

CFD Computational Fluid Dynamics

EVT Eddy Viscosity Transport

FEM Finite Element Method

HPC High Performance Computer

NDT Non-Destructive Testing

RANS Reynolds-Averaged Navier-Stokes

SA Spalart-Allmaras

SST Shear Stress Transport

SUNSPOT Stellenbosch University Solar Power Thermodynamic Cycle

1-D One-Dimensional

3-D Three-Dimensional

Symbols

a Sonic velocity . . . . . [m/s]

c	Absolute velocity	$[\mathrm{m/s}]$
c_p	Specific heat	$[\mathrm{kJ/kg{\cdot}K}]$
C	Coefficient	$[\ ]$
D	Diffusion factor	$[\ ]$
h	Enthalpy	$[\mathrm{J/kg}]$
I	Rothalpy	$[\mathrm{J/kg}]$
k	Turbulent kinetic energy	$[\mathrm{m^2/s^2}]$
L_B	Blade length	$[\mathrm{m}]$
$\dot{m}$	Mass flow rate	$[\mathrm{kg/s}]$
M	Mach number, Molar mass	$[-, \mathrm{kg/kmol}]$
N	Rate of Rotation	$[\mathrm{rpm}]$
p	Pressure	$[\mathrm{Pa}]$
P	Power	$[\mathrm{W}]$
r	Radius	$[\mathrm{m}]$
s	Entropy	$[\mathrm{J/kg{\cdot}K}]$
T	Temperature	$[\mathrm{K}]$
u	Velocity, blade speed (Ωr)	$[\mathrm{m/s}]$
U	Velocity	$[\mathrm{m/s}]$
$\tilde{v}$	Kinematic eddy viscosity parameter	$[\mathrm{m^2/s}]$
V	Free stream velocity	$[\mathrm{m/s}]$
w	Relative velocity	$[\mathrm{m/s}]$
W	Work, blade-to-blade passage width	$[\mathrm{J}, \mathrm{m}]$

x	Cartesian coordinate	[m]

Greek Letters

β	Blade angle	[rad]
η	Efficiency	[ ]
γ	Ratio of specific heats	[ ]
λ	Impeller tip distortion factor	[ ]
μ	Dynamic viscosity, head coefficient	[kg/m·s, −]
ψ	Power input factor	[ ]
Ψ	Flow coefficient	[ ]
ρ	Density	[kg/m^3]
σ	Slip factor	[ ]
θ_2	Tip flow coefficient	[ ]
ω	Turbulence frequency	[Hz]
$\bar{\omega}$	Total pressure loss coefficient	[ ]
Ω	Rotational velocity	[rad/s]

Subscripts

a	Axial
abs	Absolute
b	Bearing
CL	Clearance gap parameter
eq	Equivalent

FB	Full blade
id	Ideal
m	Meridional
MC	Disk friction – impeller cover
MD	Disk friction – impeller disk
p	Static pressure recovery
r	Radial
s	Isentropic, shroud
SB	Splitter blade
θ	Tangential
0	Total thermodynamic condition
1	Impeller inlet
2	Impeller outlet
3	Diffuser inlet
4	Diffuser outlet

Superscripts

$'$ (prime)	modified variable
$\bar{}$ (bar)	average

Chapter 1

Introduction

1.1 Background

Renewable sources of energy are playing an increasingly larger role in the energy mix of South Africa (Department of Energy, 2018). Because of its climate and geographical location, solar technologies are of particular interest.

At Stellenbosch University a small-scale concentrating solar power innovation is being interrogated for feasibility. The **S**tellenbosch **Uni**versity **S**olar **Po**wer **T**hermodynamic cycle (Figure 1.1) aims to integrate a solar thermal receiver into a Brayton cycle gas turbine upstream of the combustor (Kröger, 2011).

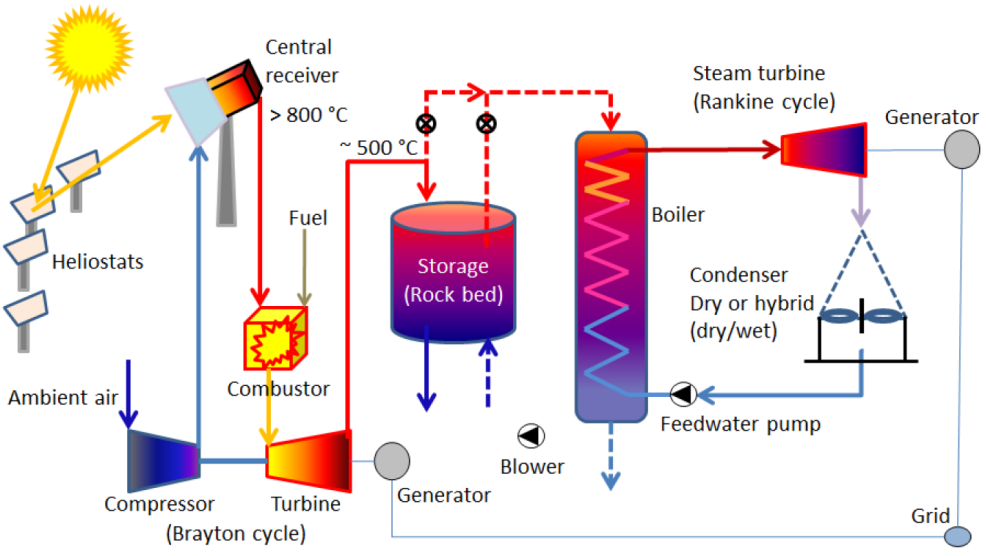

Figure 1.1: The SUNSPOT Cycle (Kröger, 2011)

In order for the system to function as envisioned, the additional pressure losses incurred by extending the cycle through the receiver need to be accounted for. Previous research has shown that this is possible by re-designing the compressor section of the Rover 1S/60 gas turbine (Homann, 2015). The re-design does not require any alteration of the turbine. Input power to the compressor, rotational speed and design point mass flow rate are all kept constant. The pressure ratio and efficiency of the compressor are improved (Luiten, 2015).

1.2 Objectives

The broad objectives for this project are three-fold. Some of these require a number of smaller sub-objectives to be met to be considered successful.

The first objective is to perform a **design review of the compressor stage**. As mentioned previously, a compressor which will improve the pressure ratio of the experimental gas turbine was already designed by Luiten (2015). This design needs to be reviewed and shown to be accurate.

The second objective of the current project is to **perform a comprehensive structural analysis** of the compressor impeller. The impeller of a gas turbine compressor experiences stresses due to the operating conditions under which it is used. It is hence vital that the following be shown:

- The structural integrity of the impeller under operating conditions needs be assured.
- With the new impeller, gas turbine operation is safe up to operating conditions and within reasonable margins.

The third major objective is to **manufacture the new compressor**. Once it has been shown from both a fluid mechanical and a structural point of view that the new compressor can perform its intended function, it needs to be manufactured. When designing for this step of the process two conditions need to be met:

- The flow channel should not be altered during manufacture.
- The existing shroud and shaft should be altered as little as possible.

1.3 Motivation

Since the start of the industrial revolution in 1750, levels of atmospheric carbon dioxide have increased by almost 38%. Methane levels have increased more than four times that much (NASA Earth Observatory, 2010). One of the primary contributing factors to the ensuing global warming is the increased rate of fossil fuel combustion, most of which takes place in the electricity and heat production industries.

Not only does this sector contribute to a quarter of all greenhouse gas emissions globally (EPA, 2017), it is also the foremost consumer of fossil fuels. Fossil fuels are being depleted rapidly, with 50% of most reserves consumed already (Asif and Muneer, 2007).

Harnessing solar energy provides an attractive resource, especially to developing countries with accessible land area and high exposure to solar radiation. South Africa is fortunate enough to count itself among such countries (Philibert, 2011) and hence alternative means of electricity production should be investigated.

The SUNSPOT cycle is a compact (in terms of CSP) cycle that integrates modern central receiver technology into the proven Brayton gas turbine cycle. Gas turbines are available in sizes ranging from 480 MW to 20 kW (Boyce, 2012). The gas turbine which is used in this project outputs 45 kW (Rover Gas Turbines Limited).

The Rover 1S/60 gas turbine is used, because of its availability for research at the Department of Mechanical and Mechatronic Engineering of Stellenbosch University. Using this turbine also demonstrates the feasibility of "up-cycling" existing (and possibly dated) technology for use in renewable energy applications. Because of the imminent threat of resource depletion it is vital that industries consider the implications of re-designing existing infrastructure to function better and more sustainably.

All of the above can be summarised when saying that the project hopes to demonstrate the feasibility of converting an existing and dated gas turbine to function efficiently in a solar thermal energy cycle.

This document will present literature relevant to the project. It will then explain the different one-dimensional models used to analyse the compressor. After that a review of a previous study's three-dimensional model will be performed. A structural analysis of the compressor will also be presented. Having established the behaviour of both the fluid and the physical part, designs will be drafted and the part manufactured. In closing some recommendations are offered.

Chapter 2

Literature Study

Gas turbines are important in both the aerospace and power generation industries. Formal analysis and design of these devices have been performed since the middle of the twentieth century. Hence a large body of literature exists. It is necessary to identify literature that is relevant to the present project.

2.1 Turbomachinery & Gas Turbine Fundamentals

Turbomachines are classified as "devices in which energy is transferred either to, or from, a continuously flowing fluid by the dynamic action of one or more moving blade rows." (Dixon, 2010). The rotating blade rows change the stagnation enthalpy of the fluid where enthalpy is understood to be the thermodynamic potential of the moving fluid. These devices can be broadly split into two categories: those that absorb power to increase fluid pressure and those that produce power by reducing fluid pressure.

Turbomachines can further be classified according to the direction in which the working fluid moves through them. If the fluid moves parallel to the axis of the rotating blade row, it is an axial flow machine. When the fluid enters the blade row flowing parallel to the axis but leaves the blade row flowing perpendicularly to the axis, the device is a radial flow turbomachine. Mixed flow machines exist where the fluid leaves the rotor at an angle such that neither its axial nor radial flow components are insignificant (Sayers, 1990).

Over the last 20 years advances in materials technology and cooling systems, as well as increases in compressor pressure ratio have increased simple-cycle gas turbine thermal efficiency from about 15% to 45% (Boyce, 2012). Gas turbines exist in a wide range of sizes and are used to address many different energy generation challenges. Different types of gas turbines, by size,

are (Boyce, 2012):

- Frame type heavy-duty gas turbines - 3 to 480 MW; efficiencies between 30% and 48%.
- Aircraft-derivative gas turbines - 2.5 to 50 MW; efficiencies between 35% and 45%.
- Industrial-type gas turbines - 2.5 to 15 MW; efficiencies in the low 30s.
- Small gas turbines - 0.5 to 2.5 MW; efficiencies between 15% and 25%.
- Microturbines - 20 to 350 kW; efficiencies vary drastically.
- Vehicular gas turbines - 300 to 1,500 HP (i.e. 223 kW to 1 120 kW); efficiencies vary drastically.

The Rover 1S/60 Gas Turbine is a microturbine. The three most important criteria when designing these units are: initial cost, efficiency and emissions. A well-designed microturbine will further be compact in in size, quiet to operate and quick to start. Most microturbines use radial flow compressors and turbines (Boyce, 2012).

2.1.1 The Rover 1S/60 Gas Turbine Engine

The Rover 1S/60 series gas turbine engine (shown schematically in Figure 2.1) can develop up to 60 HP (45 kW). It is a single shaft machine that was intended for ground use in an industrial context but found prominent application driving ship-borne fire fighting pumps and auxiliary generators on hovercraft. It was even fitted in the Vulcan B2 Bomber as an airborne auxiliary power plant (gasturbineworld, 2018).

The turbine that is owned and operated the department of Mechanical & Mechatronic Engineering of the University of Stellenbosch was previously tested by Luiten (2015) and Zhang (2016). They found that at its operating point the compressor produced a total-to-static pressure ratio of 2.60 with a mass flow rate of 0.597 kg/s.

The Rover 1S/60 uses a single stage centrifugal compressor. Its impeller is machined from a forged aluminium alloy. The impeller is press-fitted onto the compressor shaft (Zhang, 2016).

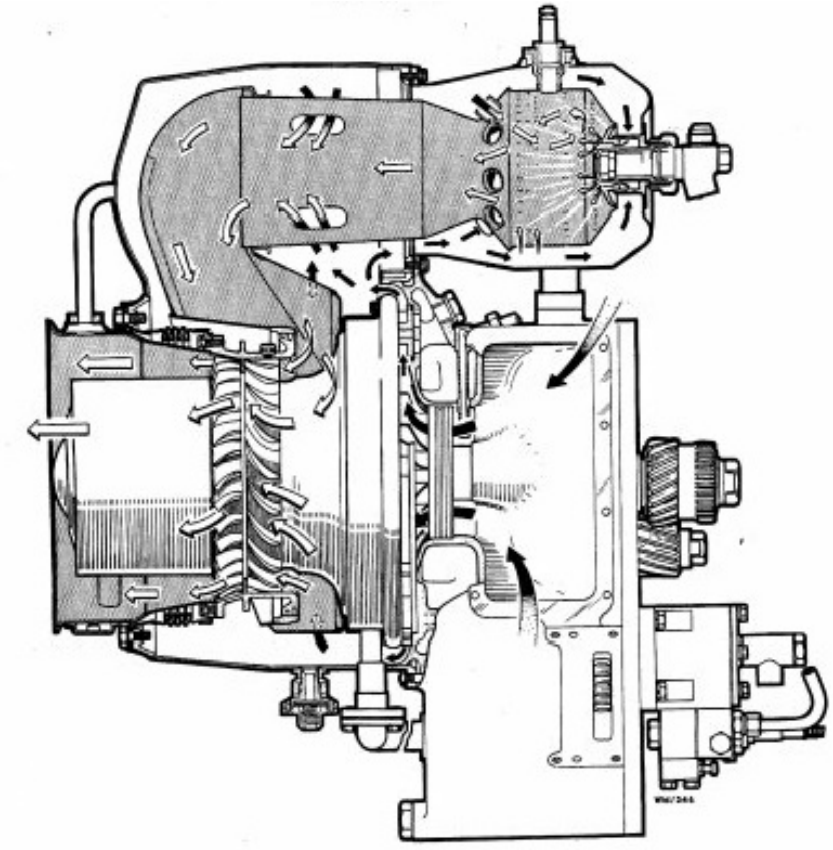

Figure 2.1: Gas Flow Diagram of Rover 1S/60 & 1S/90 type turbines (gasturbineworld, 2018)

2.1.2 Centrifugal Compressors

Compressors are devices which consume mechanical energy to pressurize a working fluid. In a centrifugal compressor the working fluid (most commonly air) enters axially and exits radially. The compressor stage consists of two parts: the impeller and the diffuser. These two components, together with a host of supplementing parts, are shown in Figure 2.2.

The impeller is the part of the compressor that imparts energy to the fluid. It has two parts: the inducer and the radial blades. The inducer is the region of the full impeller blade that can be compared to an axial-flow rotor. It begins at the leading edge and increases the fluid's angular momentum while maintaining a relatively constant radius in the flow direction (Boyce, 2012). The impeller section of the blade facilitates radial motion of the fluid. In this region a large increase in radius is seen.

Due to vastly different flow conditions at the hub and shroud surfaces of the impeller, flow patterns at these surfaces are complex and different. According

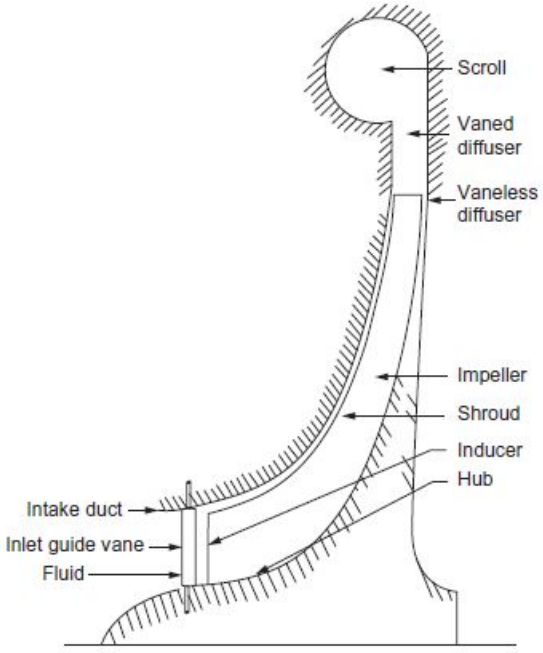

Figure 2.2: Schematic of a Centrifugal Compressor (Boyce, 2012)

to Boyce (2012) experimental studies of flow in impeller channels have shown velocity profiles that differ from those predicted using theoretical models.

In the diffuser, the kinetic energy imparted to the fluid by the impeller is recovered and converted into pressure (Boyce, 2012). A typical vaned diffuser relies on two mechanisms to achieve this. The effect of passage area is also seen in vaneless diffusers and is inherent to centrifugal compressors due to the increase of radius in the flow direction. Augmenting this is the blade loading or fluid turning effect. Matching the rotational impeller to a optimal, functional diffuser is complicated, because "the flow path changes from a rotating system into a stationary one" (Boyce, 2012).

Fluid leaving the diffuser is at a high static pressure. It now enters a scroll, volute or collector in which it will be further manipulated. The volute increases the static pressure further and links the outlet of the diffuser to the next part in the machine. In the case of the Rover gas turbine this is the combuster.

2.2 Velocities

Because of the nature of turbomachines, it makes sense to use a polar coordinate system to describe the machine and analyse it. The coordinate system's z-axis is usually aligned with the axis of rotation of the machine. Flow in a turbomachine has varying velocities in all three directions. To simplify

analysis it can be assumed that the flow velocity in the tangential direction remains constant. Under this condition flow moves through the machine on a axi-symmetric stream surface with a meridional velocity component which is defined as in equation 2.2.1 (Dixon, 2010).

$$c_m = \sqrt{c_a^2 + c_r^2} \tag{2.2.1}$$

A frame of reference which appears stationary relative to the rotating turbomachinery simplifies analysis of the flow field in this region (Dixon, 2010). Descriptions for relative velocities are related to absolute velocities as per

$$w_\theta = c_\theta - \Omega r, w_a = c_a, w_r = c_r. \tag{2.2.2}$$

Velocities in the absolute frame of reference are designated by c and those in the relative frame by w. Subscript m indicates meridional components, subscript θ tangential ones. Using relative velocities when re-writing equation the expression for rotational stagnation enthalpy (equation A.3.4 of Appendix **??**) provides, after addition and subtraction of $\frac{1}{2}U^2$, equation 2.2.3.

$$h_2 - h_1 = \frac{1}{2}(U_2^2 - U_1^2) + \frac{1}{2}(w_1^2 - w_2^2) \tag{2.2.3}$$

Equation 2.2.3 demonstrates how the change in radius contributes to the rise of static enthalpy in a centrifugal compressor's impeller. The first term on the right of the equal sign represents the part of the enthalpy rise that is due to an increase in radius.

The description of flow field velocities relates closely to fundamental thermodynamic laws (Appendix A). An example of this is the momentum equation (section A.3). The momentum equation (equation A.3.1) relates external forces acting on a fluid element in the axial direction to the acceleration of that same element in the axial direction.

Under the assumptions that gas viscosity and thermal conductivity are zero, equation A.3.1 can be adapted for compressible, inviscid flow in a rotating coordinate system. Expanding the total derivative, manipulating algebraically and introducing the definitions of stagnation enthalpy, entropy (equation A.4.2), rothalpy (equation A.3.4) and total enthalpy in rotating systems equation 2.2.4 is obtained (Aungier, 2000).

$$\frac{\partial \vec{w}}{\partial t} - \vec{w} \times (\nabla \times \vec{w} + 2\vec{\Omega}) = -\nabla I + T\nabla s \tag{2.2.4}$$

In the above expression the substantial time derivative of relative velocity (w) is related to the sum of rothalpy (I) and entropy's (s) gradients. Temperature and the rotational speed, T and Ω respectively, influence this relationship. The equations for continuity and energy can be expressed in vector form too. Forms of the fundamental thermodynamic laws which are suitable for the study of turbomachinery are developed by both Dixon (2010) and Aungier (2000).

2.3 Preliminary Design

Impellers and diffusers require individual attention and the need to clearly relate performance targets to geometric properties exists.

2.3.1 The Impeller

Discussions of preliminary compressor design are best initialised by analysing the impeller work input coefficient. This indicates the total rise in fluid enthalpy during passage through the impeller. It is defined in equation 2.3.1. In the same equation the major contributing work and loss coefficients are presented.

$$I = \frac{\Delta h_0}{u_2^2} = I_B + I_{DF} + I_L + I_R \tag{2.3.1}$$

The different work coefficients represented in equation 2.3.1 are:

- I_B - blade work input; useful work done by the impeller
- I_{DF} - windage and disk friction; friction caused by fluid caught between impeller and housing
- I_L - leakage; flow from the impeller discharge to the inlet through the eye seal
- I_R - recirculation; flow re-entering the impeller at the tip

Individual coefficients can be calculated, if certain properties are known. The blade work, for example, follows from the Euler turbine equation. For an infinite amount of infinitesimally thin blades this can be written as

$$I_B = (1 - \lambda\phi_2 cot\beta_2) - u_1 c_{\theta 1}/u_2^2 \tag{2.3.2}$$

where λ, the distortion factor, is related to the tip area blockage. The latter increases with aspect ratio, velocity head diffusion from blade throat to passage discharge and blade clearance (Aungier, 2000).

Likewise, the disk friction work, I_{DF}, is calculated by drawing on the work of Daily and Nece (1960). Any enclosed disk (a disk rotating in a fully closed chamber and whose motion only affects a finite volume of fluid) experiences one of four flow regimes. Through theoretical analysis Daily and Nece (1960) were able to formulate torque coefficient expressions for each flow regime. The different regimes are described by combinations of the Reynolds number and the ratio of axial clearance and radius. Empirical equations confirm the accuracy of the the theoretical equations. Only after calculating the coefficient for every regime can the correct one be chosen – the one yielding the greatest torque value. By applying a correction for gap leakage flow and separating torque coefficients for the impeller disk and cover (should one exist) an expression for disk friction work can be produced (Aungier, 2000).

$$I_{DF} = (c_{MD} + c_{MC})\rho_2 u_2 r_2^2/(2\dot{m}) \tag{2.3.3}$$

The biggest difference between open and covered impellers is with regards to leakage flow behaviour. Leakage losses are only important for covered impellers and depend on the geometry of the eye seal. An analogous property in open impellers is blade/housing clearance gap flow. This flow occurs, because of the pressure difference across the blade's two sides. The velocity of this flow (u_{CL}) can be estimated by the product of a throttling coefficient and the square root of the average pressure difference. The average pressure difference is estimated from the change in fluid angular momentum through the impeller and the throttling coefficient is computed by assuming first abrupt contraction and then abrupt expansion in the direction of the leakage flow (Aungier, 2000). From the leakage flow velocity and the clearance gap width an expression for the total leakage mass flow ($\dot{m}_{CL}$) can be developed. Half of this stream re-enters the blade passage and is re-energised which is accounted for by the leakage work coefficient, I_L.

$$I_L = \dot{m}_{CL} u_{CL}/(2u_2\dot{m}) \tag{2.3.4}$$

Recirculation losses contribute to total work input in impellers with a high head coefficient, excessive blade loading and low relative tip flow angles (Aungier, 2000). A generalization of the equivalent diffusion ratio is used to calculate these losses. For axial compressor cascades Lieblein (1959) showed that a loss in total pressure can be estimated from the design suction surface diffusion ratio $V_{max,s}/V_2$. V here represents free stream velocities. For use in

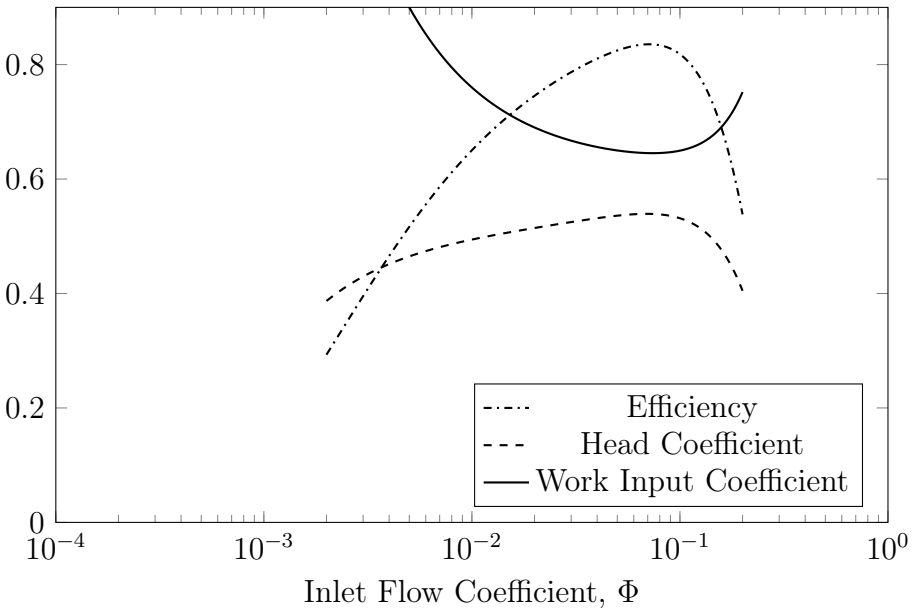

Figure 2.3: Performance Targets for Open Impellers with Vaned Diffusers (adapted from Aungier (1995*a*))

the design process he established an equivalent ratio, D_{eq}, which is based on inlet and outlet conditions rather than surface velocity data. Aungier (1995*b*) generalized the ratio for use in centrifugal compressors: $D_{eq} = W_{max}/W_2$. Upon finding the stall limit expression of Lieblein (1959) appropriate too, Aungier (1995*b*) defined the recirculation work coefficient as:

$$I_R = (D_{eq}/2 - 1)(w_{\theta 2}/c_{m2} - 2\cot\beta_2) \tag{2.3.5}$$

Compressors using open impellers and vaned diffusers are expected to produce work coefficients similar to those shown in figure 2.3. For the purpose of the preliminary design, the work input coefficient, also plotted in figure 2.3, is defined as μ_p/η_p and related to the stage flow coefficient θ using expressions developed by Aungier (1995*a*).

In a centrifugal compressor without guide vanes the flow has no whirl at the inlet. The specific work (equation A.3.3) simplifies to the following equation.

$$\Delta W = \Omega r_2 c_{\theta 2} \tag{2.3.6}$$

At the inlet of the impeller it is important to avoid large relative velocities. These can increase pressure losses or produce Mach number effects. Suitable impeller eye sizing ensures that optimal flow conditions exist at the inlet. Such

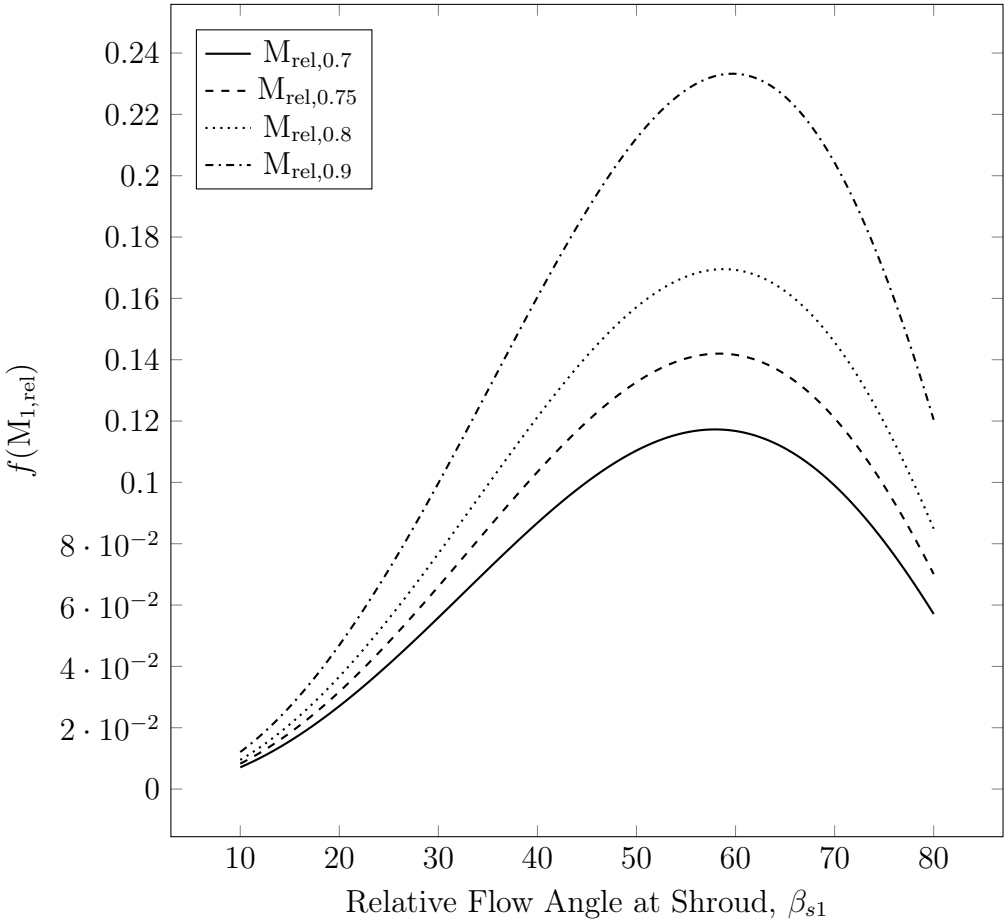

Figure 2.4: $f(\mathrm{M}_{1,\mathrm{rel}})$ against β_{s1} for Different Relative Mach Numbers (Dixon, 2010)

conditions limit the relative Mach number while ensuring high efficiencies. Dixon (2010) demonstrates how to size an impeller eye for axial inlet flow. His approach allows the designer to choose a relative inlet Mach number as the limit. It then relates optimum blade angle and maximum mass flow as per Figure 2.4.

The relative Mach number, $f(\mathrm{M}_{1,\mathrm{rel}})$, is defined as in equation 2.3.7 (Dixon, 2010). Note that it describes mass flow rate as the only variable. At the design point, and with certain geometric constraints all other properties are known. The constant k is a function of the hub and shroud radii.

$$f(\mathrm{M}_{1,\mathrm{rel}}) = \frac{\dot{m}\Omega^2}{\pi k p_{01} a_{01}^3} \tag{2.3.7}$$

Another method sets the desired relative inlet flow angle and proceeds from

there. A flow angle which would minimize, approximately, the relative inlet velocity w_1 is 30° (Aungier, 2000). This is the rms inlet blade angle and it results — for a compressor with a geometry similar to that used in the current project — in a relative Mach number at the shroud of approximately 0.76. This value is comparable to the relative Mach number recommended for most industrial applications by Dixon (2010).

To design the impeller outlet a designer may chose to let the radial velocity component equal the axial velocity component at impeller entry (Dixon, 2010). With the tangential velocity component known — it is the product of impeller outlet radius, rotational velocity and slip factor — a total impeller outlet velocity and outlet flow angle can be calculated.

Alternatively empirical expressions can be used to calculate the outlet flow angles (Aungier, 2000). To achieve a wide stable operating range and good performance, small outlet flow angles are desired.

Once inlet and outlet flow angles have been determined, the impeller blade needs to be defined. To do this a designer can use straight-line surface elements to connect the hub and shroud curves. Aungier (1995*a*) provides descriptions for curves in terms of the normalized meridional distance. To control the blade rake angle he uses a parameter K when describing the hub curve. The hub contour, on the other hand, is designed to fit the largest permitted arc (Aungier, 1995*a*). If needed, linear extensions can be used at the inlet and outlet of the impeller to fit the hub's circular arc. Corresponding shroud contours are defined using three-point cubic spline fit curves. In cases where linear extensions are used on the hub it is advisable to use the corresponding extensions for the shroud curve (Aungier, 1995*a*).

2.3.2 The Diffuser

Impeller-diffuser interaction has a profound effect on the performance of a compressor stage. Leakage flow at the impeller tip is influenced most by the interaction of the two parts. The effects of the interaction are already manifested in the impeller and affect slip velocity (Shum *et al.*, 2000). The radius ratio describes the interaction of the two parts and has the potential to reduce blockage and slip, and lower the increase of losses as it increases (up to a point). The ideal radius ratio has a value between 1.06 and 1.10 (Clements and Artt, 1989).

Conventional diffusers use thin blades, but due to assembly requirements these are not a viable option for the current project. In order to accommodate the mounting bolts at the correct radius, thick, island-style vanes are used.

From the average blade-to-blade velocity difference — related to the change

in angular momentum — and the requirement that, at operating point, the blade angles equal the flow angles, a blade loading parameter can be defined (Aungier, 2000). This parameter is an approximation of the vane-to-vane pressure difference over inlet-to-outlet pressure difference ratio.

Aungier (2000) proposes that pressure recovery in the diffuser matches discharge area blockage (B_4) for isentropic flow which is perfectly guided by the diffuser vanes. Blockage is related to skin friction and diffusion by equation 2.3.8.

$$B_4 = [K_1 + K_2 (D - 1)] L_B / W_4 \tag{2.3.8}$$

This expression is developed from the analysis of 18 experimental diffusers. It is shown that, with some modification, it is applicable for almost all diffuser shapes and types (Aungier, 2000). L_B is the blade length and W_4 is the effective blade-to-blade passage width at the outlet. The equivalent divergence angle is contained in the definition of K_2. K_1 is an adjusted blockage correction factor (Aungier, 2000).

2.4 One-Dimensional Performance Analysis

Once a preliminary design of the compressor's components has been completed, the flow along a mean stream surface is analysed. Empirical fluid dynamics and loss coefficients are used to supplement theoretical methods. The model used and the analysis of the flow therein are inseperable, because the developers of the model can not validate their models individually (Aungier, 2000).

2.4.1 The Impeller

An understanding of the impeller's work input (section 2.3.1) is critical to the performance analysis thereof. This process begins with the known, total inlet flow conditions. Equations 2.2.2 and A.3.4, together with the definition of relative total enthalpy in rotating coordinates (Aungier, 2000) allow the formulation of an expression which solves for relative total enthalpy at the inlet. In the rotating frame of reference, rothalpy is conserved (see section A.3) and hence the impeller outlet enthalpy can be calculated (equation 2.4.1) (Aungier, 2000).

$$h'_{02} = h'_{01} + (U_2^2 - U_1^2)/2 \tag{2.4.1}$$

The prime notation in equations 2.4.1 and 2.4.2 denotes a relative condition in the rotational frame of reference. Ideal, relative, total conditions at the

impeller outlet can be computed from equation 2.4.1. These ideal conditions can be corrected using loss coefficitnets provided that the total pressure loss is known. Loss coefficients are, however, based on inlet conditions, but applied at the outlet and it becomes necessary to correct them to ensure that the entropy rise previously calculated for the impeller is not changed. Aungier (2000) shows that, by applying equation A.4.2, equation 2.4.2 can be constructed. In this equation f_c is the correction factor that preserves an the entropy rise.

$$p'_{02} = p'_{02id} - f_c(p'_{01} - p_1)\sum_i \bar{\omega}_i \tag{2.4.2}$$

The accuracy of the equation will vary with pressure ratio if the correction factor is not applied. Such behaviour is unique to the impeller. In the diffuser (which is a stationary component) total pressure loss throughout is invariant (Aungier, 2000).

The analysis process according to Aungier (2000) iteratively solves for blade work and losses until the impeller mass flow has converged. This process is explained more elaborately by Figure 2.5. The loss models referenced in Figure 2.5 are described in Aungier (1995*b*).

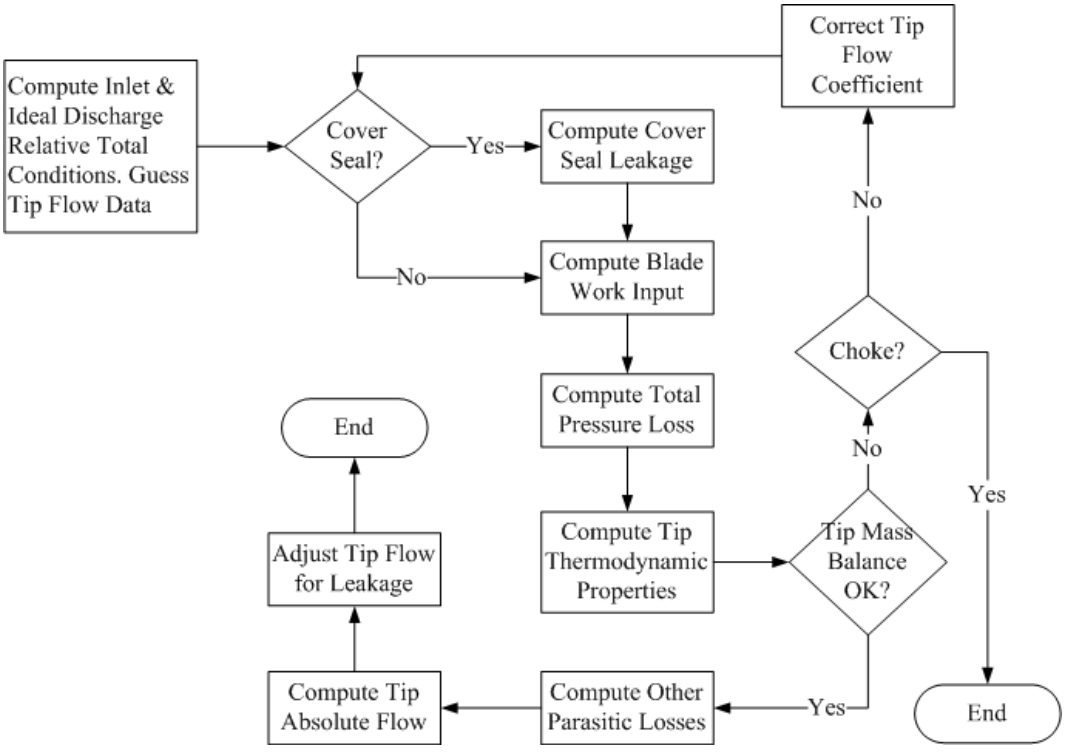

Figure 2.5: Flow Chart of Impeller Analysis (adapted from Aungier (2000))

Once the analysis has converged the total enthalpy and absolute velocity at the impeller outlet are calculated. Other thermodynamic properties can be calculated using the equation of state and isentropic calculations between h and h_t (Aungier, 2000).

2.4.2 The Diffuser

The purpose of the diffuser is two-fold: maximum kinetic energy recovery with minimum loss of total pressure. These traits are subsequently what the performance of the diffuser is judged by.

The rise in static pressure through the diffuser is commonly divided by the diffuser inlet dynamic pressure to define a static pressure recovery coefficient. Equation 2.4.3 illustrates this and subsequently provides a means of thinking about the fundamental purpose of a diffuser (Japikse and Baines, 1989).

$$C_p = \frac{p_4 - p_3}{p_{03} - p_3} \tag{2.4.3}$$

Similarly an ideal pressure recovery coefficient can be calculated (equation 2.4.4). This value is a useful reference from which some functional relationships can be deduced (Japikse and Baines, 1989). To calculate the ideal pressure recovery coefficient only flow velocities at the diffuser inlet and outlet need to be known. It is possible to express the velocity fraction as an area ratio.

$$C_{p,id} = 1 - \frac{U_4^2}{U_3^2} \tag{2.4.4}$$

In dividing one with the other, the real and ideal static pressure recovery coefficients express the diffuser effectiveness. The diffuser effectiveness is useful when performance needs to be estimated under conditions unknown relative to available data (Japikse and Baines, 1989). The diffuser efficiency under compressible flow conditions, for example, can be expressed by equation 2.4.5 (Krige, 2013).

$$\eta = \left[\left(\frac{p_4}{p_3} \right)^{\frac{\gamma-1}{\gamma}} - 1 \right] \frac{T_3}{T_4} - T_3 \tag{2.4.5}$$

Likewise a total pressure loss coefficient can be calculated by dividing the difference of the integrated mass-averaged inlet and outlet total pressures with the integrated mass-averaged diffuser inlet dynamic pressure as in equation 2.4.6.

$$C'_{p0} = \frac{\bar{p}_{03} - \bar{p}_{04}}{\bar{p}_{03} - \bar{p}_3} \tag{2.4.6}$$

This loss coefficient refers to the entire flow field because the diffuser is a basic dynamic element in a larger system. Relating the total pressure loss to the static pressure recovery coefficient, $C'_{p0} = C_{p,id} - C_p$, is fundamental to the formulation of diffuser loss maps. Experimental data plotted on such a map allows one to determine deviations from the ideal (Japikse and Baines, 1989). Inlet Mach number, aerodynamic blockage, incidence angle and solidity have the most prominent effect on the performance of a vaned diffuser (Krige, 2013).

2.5 Turbulence Models

Highly disordered flow which is characterised by velocity fluctuations is referred to as turbulent (Çengel, 2014). In such flows the Reynolds number (Re) exceeds the critical Reynolds number (Re_{crit}). Turbulent flow behaviour is typically described by decomposition into a mean value which has a fluctuating component superimposed onto it. These fluctuations always have a three-dimensional spatial character. Eddies, rotational flow structures, are also seen in turbulent flows (Versteeg and Malalasekera, 2007). In most common engineering applications it is, however, not necessary to resolve these features. Various procedures based on the Reynolds-averaged Navier-Stokes (RANS) equations are used instead. Some of these procedures are described in the following sections.

2.5.1 The Boussinesq Approximation

An eddy viscosity model is defined by the assumption that Reynolds stresses are proportional to mean velocity gradients (Versteeg and Malalasekera, 2007). The two are related by the gradient diffusion hypothesis (equation 2.5.1). In ANSYS CFX this model is called the eddy viscosity transport (EVT) equation.

$$-\rho\overline{u'_i u'_j} = \mu_t \left(\frac{\partial U_i}{\partial x_j} + \frac{\partial U_j}{\partial x_i} \right) - \frac{2}{3}\delta_{ij} \left(\rho k + \mu_t \frac{\partial U_k}{\partial x_k} \right) \tag{2.5.1}$$

The parameter of interest is μ_t – the eddy viscosity. By division with the Prandtl number, eddy viscosity can be related to eddy diffusivity. The latter is a means of turbulence description that is analogous to the eddy viscosity hypothesis.

Through use of these hypotheses and by definition of an effective viscosity $\mu_{eff} = \mu + \mu_t$ the Reynolds averaged momentum and scalar transport equations can be modified (ANSYS Inc., 2018*b*). A modified pressure can now be defined (see equation 2.5.2). By default, when p is required, CFX approximates it as p'.

$$p' = p + \frac{2}{3}\rho k + \frac{2}{3}\mu_{eff}\frac{\partial U_k}{\partial x_k} \tag{2.5.2}$$

2.5.2 The k-ω Turbulence Model

This model solves the turbulent kinetic energy (k) and the turbulent frequency (ω) of the flow. These two properties are related to turbulence viscosity by the relation presented in equation 2.5.3.

$$\mu_t = \rho\frac{k}{\omega} \tag{2.5.3}$$

Equation 2.5.3 illustrates the greatest flaw of the basic k-ω model. As ω tends to zero in the free stream, the eddy viscosity becomes infinite. Hence as small, non-zero viscosity value must be prescribed when solving flow in the free stream. Results depend strongly on this prescribed value (Versteeg and Malalasekera, 2007).

2.5.3 The Shear Stress Transport (SST) k-ω Turbulence Model

The deficiency of the normal k-ω model is addressed by the SST k-ω model. Near the wall this model uses the robust and accurate k-ω model which was discussed previously. In the outer part of the boundary layer, however, it takes advantage of the k-ϵ model's free stream independence by transforming it to a k-ω formulation (Menter, 1994). To facilitate the transition the original model is multiplied by the blending function F_1 and summed with the product of the transformed model and $(1 - F_1)$. F_1 is one at the wall and zero in the free stream.

To further refine the model and predict the onset and amount of flow separation more accurately, a limiter is introduced in the eddy viscosity equation. This is shown in equation 2.5.4

$$\mu_t = \frac{A_1\rho k}{\max\left(A_1\omega, F_2\sqrt{\frac{1}{2}\left(\frac{\partial U_i}{\partial x_j} + \frac{\partial U_j}{\partial x_i}\right)\left(\frac{\partial U_j}{\partial x_i} + \frac{\partial U_i}{\partial x_j}\right)}\right)} \tag{2.5.4}$$

where A_1 is a constant and F_2 is a blending function (Versteeg and Malalasekera, 2007). The blending function takes as arguments the turbulent kinetic energy, the turbulent frequency, the distance to the nearest wall and the eddy viscosity.

Calculating the blending functions and an additional cross-diffusion term is the price for free stream independence and improved eddy viscosity behaviour. This cost is, however, negligibly small and overall computing time and stability are unaffected (Menter, 1994).

2.5.4 The Spalart-Allmaras (SA) Turbulence Model

Unlike the k-ω models, the SA model solves a single transport equation for the kinematic eddy viscosity parameter $\tilde{v}$ and algebraically sets a length scale for the blocking effect of the wall (Spalart and Allmaras, 1994). This makes it more economic than the two equation models previously described (Versteeg and Malalasekera, 2007).

The kinematic eddy viscosity is related to the dynamic eddy viscosity as shown in equation 2.5.5. Near the wall the wall damping function f_{v1} tends to zero and for high Reynolds numbers it approaches unity. The latter means that, at high Reynolds numbers, the kinematic eddy viscosity parameter is equal to kinematic eddy viscosity. The length scale used in the SA model is the denominator of the destruction term of the transport equation for the kinematic eddy viscosity parameter. It is equal to the mixing length used to develop log-law boundary layers (Versteeg and Malalasekera, 2007).

$$\mu_t = \rho \tilde{v} f_{v1} \tag{2.5.5}$$

The SA model performs well for flows with boundary layers experiencing adverse pressure gradients. Complex geometries, however, make the specification of the length scale difficult. This means that the model is not suitable for general internal flows (Versteeg and Malalasekera, 2007).

2.6 Rotor Dynamics

Forced vibrations are of interest in the field of turbo-machinery. If the exciting frequency — typically the speed of the shaft — coincides with one of the system's natural frequencies, resonance is encountered and dangerously large amplitudes can occur. Lacking other applied periodic loads, the unbalances assumed to exist in all rotating machinery produce excitations of the same frequency as the rotational speed (Boyce, 2012). When the frequency of rotation

equals the natural frequency (excluding damping), the amplitude ratio reaches a maximum.

Damping, however, can come from several sources in the system. Parts moving through a fluid typically encounter viscous damping. Sliding surfaces produce friction damping, and internal friction causes solid damping. The effect of all these phenomena is proportional to the velocity of the body and reduces the natural frequency ω_n which in turn is the square root of spring stiffness divided by mass (Inman, 2014).

Knowledge of these characteristics and how they relate to one another allows the design of small machines which operate at speeds well below their natural frequencies (Boyce, 2012). Decreasing the size of the machine decreases the mass which in turn serves to increase the natural frequency. If the operating speed is now sufficiently slow it is unlikely that the applied frequency will match the natural one.

A large disc on a flexible shaft mounted to flexible supports is the most simple method of modelling a rotor mounted to a shaft on bearings. The natural frequency of such a system is represented by equations 2.6.1.

$$\omega_{nt} = \omega_n \sqrt{\frac{K_b}{K_b + K_r}} \tag{2.6.1}$$

K_r is the radial stiffness of the shaft which acts to counter the displacement of the mass. The natural frequency ω_n is that of the same rotating disc and shaft when mounted on rigid supports (Boyce, 2012).

An Aluminium impeller will typically have a lower stiffness than a shaft made of steel and subsequently lower natural frequencies. Hence the impeller's vibrational behaviour needs to be considered. This single part, due to its shape and material can have multiple natural frequencies. The number of natural frequencies equals number of degrees of freedom of the system (Inman, 2014). Mode shapes are used to describe the relative motion between multiple degrees of freedom. Such a modal analysis presents all the natural frequencies of a machine component (ANSYS Inc., 2018*c*).

The first step of a modal analysis is to solve the undamped eigenproblem. In this manner lower frequencies and modes of the structure are obtained. Then a value for modal displacement is found using the generic modal equation (Cook *et al.*, 2002). Modal displacement is related to physical displacement by the matrix of eigenvectors. Phase angles can be found using software to search for the correct frequency of excitation around a natural frequency (Cook *et al.*, 2002).

Chapter 3

One-Dimensional (1-D) Fluid Mechanical Modelling

The one-dimensional design was undertaken to establish a baseline for fluid mechanical analysis. It was also used as a means of reviewing the 1-D design done by Luiten (2015). Performance parameters for various compressor components as designed by Luiten (2015) are known. Parts of the process he used are also known. The expectation is that, with this information, his design can be replicated. The present 1-D model hence strives to match the values achieved by Luiten (2015)

3.1 Dixon Model

This analytical model is based on a method described by Dixon (2010) and is henceforth referred to as the "Dixon" model. It is writtern in Python on the PyCharm Communtiy IDE (see Appendix B) and applies fundamental 1-D compressor design theory. The initial values are shown in Table 3.1. Locations at which calculations are performed are shown in Figure 3.1.

Table 3.1: Dixon Model: Known Conditions

Property	**Symbol**	**Value**
inlet pressure	$p_{01} \times 10^3$	101.325
inlet temperature	T_{01}	293
mass flow rate	$\dot{m}$	0.6
rate of rotation	N	46000
number of full blades	z_{FB}	12
number of splitter blades	z_{SB}	12
meridional length ratio	L_{SB}/L_{FB}	0.7
maximum compressor radius	r_4	0.132

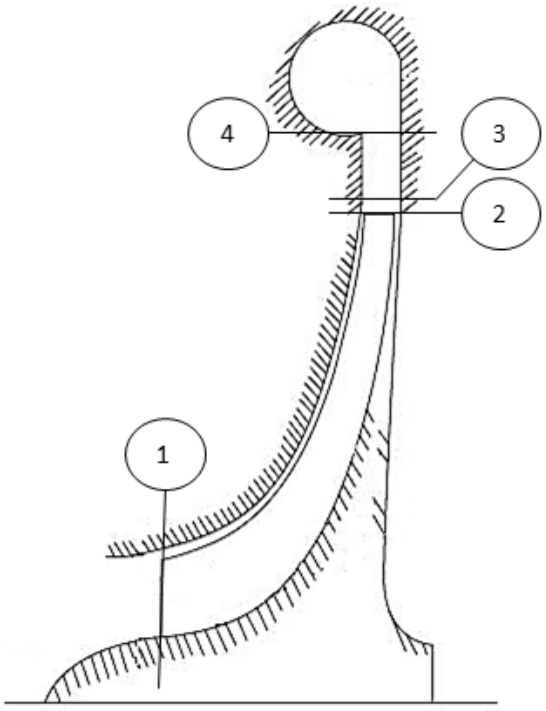

Figure 3.1: Locations where calculations are performed

Dixon (2010) uses a known number of full blades in his approach. An equivalent blade number, calculated using equation 3.1.1, was used instead (Aungier, 2000). Furthermore, the specific heat, specific heat ratio and gas constant for air were used. These properties have values of 1.055 kJ/kg·K, 1.4 and 0.287 kJ/kg·K respectively.

$$z = z_{FB} + z_{SB} * \frac{L_{SB}}{L_{FB}} \tag{3.1.1}$$

Dixon (2010) recommends using a suitable relative Mach number at the shroud when designing the impeller inlet. Changing the relative Mach number influences design behaviour, but after iteration, M_{rel} was chosen to be 0.7. This also corresponds to "the normal range used in practice" (Dixon, 2010).

The analytical model starts by calculating the impeller outlet radius. This is calculated from the rotational velocity which is a function of input power, mass flow rate and slip factor. Here the Stanitz expression (equation 3.1.2) is used to calculate the slip factor for an impeller with a known number of blades z.

$$\sigma = 1 - \frac{0.63\pi}{z} \tag{3.1.2}$$

Next the stagnation speed of sound at the inlet is determined. This, together with β_{max} — the value of β_{s1} which results in a maximum on the left-hand side of equation 3.1.3 for the chosen $\mathrm{M}_{1,\mathrm{rel}}$ — is used to calculate the inlet radius ratio k.

$$f(\mathrm{M}_{1,\mathrm{rel}}) = \frac{\mathrm{M}_{1,\mathrm{rel}}^3 \sin^2 \beta_{s1} \cos \beta_{s1}}{1 + \frac{1}{5}\mathrm{M}_{1,\mathrm{rel}}^2 \cos^2 \beta_{s1}} \tag{3.1.3}$$

The maximum flow angle is further used to determine the absolute Mach number at the impeller inlet. From this the absolute inlet flow velocity can be determined which in turn informs the shroud radius. Having previously calculated the the inlet radius ratio the hub radius can be found too.

It is necessary to assume an efficiency to determine properties at the impeller outlet. Dixon (2010) believes an isentropic efficiency of 92% to be reasonable. For this model an isentropic efficiency 90% was used. It should be noted here that CENCOM calculates an efficiency of 89.82% for this component.

The efficiency, together with the ratio of total temperatures between impeller outlet and inlet, allows calculation of the ratio of total isentropic impeller outlet temperature and total impeller inlet temperature (T_{02s}/T_{01}). This is used to find the total-to-total pressure ratio across the impeller. From this the Mach number and the density at, and the width of the outlet are calculated.

For the next step the designer needs to decide what the radius ratio across the vaneless diffuser is. He also decides here whether the width of the vaneless diffuser remains constant. Cumpsty (1989), according to Dixon (2010), recommends a minimum ratio, r_3/r_2, of 1.1. The width of the diffuser was also taken to be equal to the blade width at the impeller outlet. Now an initial flow velocity at the inlet of the vaned diffuser can be calculated. This has an effect on the temperature and pressure at the inlet of the vaned diffuser, and hence the density. It is necessary to calculate density and velocity iteratively. Once the velocity value has converged to within a millionth, it is taken to be the diffuser inlet velocity value.

Conditions at the vaned diffuser outlet are based on an assumed total-to-total isentropic efficiency for the diffuser stage. Dixon (2010) suggests that 87.5% efficiency is "close to the maximum efficiency condition for this type of diffuser." For this phase of the present study an efficiency of 85% is selected.

It was later found, using CENCOM, that this component has an efficiency of 81.76%.

Knowledge of the diffuser geometry allows the calculation of an ideal pressure rise coefficient. After calculating the real pressure rise coefficient, the pressure and velocity at the diffuser outlet can be determined. Now various properties are known throughout the compressor and it is instructive to compare them to the same values as calculated by CENCOM (shown in Table 3.3).

3.2 CENCOM Model

Luiten (2015), however, did his 1-D design using the commercial software package CompAero. It was decided that, to ensure accuracy in the current study, the software should be used as a second 1-D design model.

Initial design data is entered into the CompAero program SIZE. Required data includes design rotational speed, impeller tip velocity, inlet temperature and pressure, head coefficients and efficiencies among others. Toggles for design properties are also available. These determine whether splitter blades will be used, whether the efficiencies should be calculated adiabatically or polytropically and if an inducer is to be designed. Program SIZE, after successfully executing, can generate input files for programs CENCOM and VDDESIGN which are also part of the CompAero package.

The input generated by program SIZE can be edited in CENCOM. The program provides extensive performance and geometry data at every important point in the compressor (see Figure 3.1). This data is then compared to the data given by Luiten (2015) and where large discrepancies are seen research into the cause thereof is done. With the knowledge thus acquired attempts are made to create a better agreement between Luiten's data and that of the current design. Where this process failed, design/analysis iterations are performed to determine the best possible fit. These iterations are recorded in Microsoft Excel.

3.2.1 Process

The primary objective when re-creating the impeller design is to match the outlet temperature to the one specified by Luiten (2015). After performing the changes described below the impeller outlet total temperature (T_{02}) is 439 K. This is 1.11% lower than the target value (443.91 K). It is, however, considered sufficiently accurate in the context of a design review.

Choking at flow rates higher than design point had to be addressed first. An iterative investigation revealed that the choking occurred in the diffuser and

was caused by a sharp bend in the vanes. The vane profile was modified. The resulting static outlet pressure is lower than that recorded by Luiten (2015), but choking up to a flow rate of 0.645 kg/s is prevented.

The largest differences with target values are observed for work coefficients. Attempts were made to adjust the recirculation work coefficient by adjusting the blade tip angle. A back-swept blade offered the closest match to the target value, but this reduced the outlet temperature. The closest temperature match was achieved with a slightly forward-swept blade which in turn led to a further deviation from the target recirculation work coefficient. In the end radial blades were chosen. This results in a recirculation coefficient of 0.01 which is 334.78% larger than the value specified by Luiten (2015).

The next largest discrepancy between Luiten's model and the present study is the disk friction work coefficient. For this coefficient the present study calculates a value of 0.0144 at the design point whereas a value of 0.0071 is presented in previous work (Luiten, 2015). This difference exists despite the fact that all surface finishes are set to "smooth." The disk friction coefficient is, by its relation to the torque coefficient, proportional to the wall roughness.

The next highest discrepancy compared to target values is observed for the distortion factor. Aungier (2000) formulated an equation to describe this factor based on his extensive experimental work, but of more value to the present investigation is the behaviour he described. The present study found the following to be of particular importance:

- The distortion factor increases with velocity head diffusion from the throat to the passage discharge.
- The distortion factor for an open impeller increases with blade clearance.

Both properties were used to reduce the distortion factor to its current value of 1.4915. This is 20.37% smaller than the target value. Velocity head diffusion was manipulated by changing the mid-passage rms blade angle. Blade clearance was reduced by changing the shroud cover clearance.

The last factor that received attention during the one-dimensional design was the leakage work. When designing for this factor multiple graphs by Egli are used (Aungier, 2000). To re-create the design of Luiten (2015) an iterative method was used. Seal parameters such as shroud/cover clearance, shaft clearance and number of fins were changed until the leakage work was 6.25% smaller than the target value.

3.2.2 CENCOM Comparison

After following the process described in section 3.2.1, the overall compressor stage performance is compared to data given by Luiten (2015). This comparison is shown in Table 3.2.

Table 3.2: Comparison of CompAero Model and Luiten (2015)

Property	**Units**	**Luiten**	**CENCOM**
Mass Flow Rate	[kg/s]	0.6	0.6
Discharge Static Pressure	[kPa]	325.97	312.92
Discharge Total Temperature	[K]	443.91	439
Discharge Flow Coefficient	[-]	0.0285	0.0279
Total-to-Static Pressure Ratio	[-]	3.25	3.09
Adiabatic Head Coefficient	[-]	0.84	0.7442
Adiabatic Total-to-Total Efficiency	[-]	0.8854	0.7862
Polytropic Head Coefficient	[-]	0.87	0.7739
Polytropic Total-to-Total Efficiency	[-]	0.8854	0.8176
Input Power	[kJ/kg]	144.57	147.69

From Table 3.2 it is clear that the new design is somewhat inferior to that performed by Luiten (2015). This can be attributed to a single factor. Not all input parameters used by Luiten (2015) are known. CENCOM is a complex software package that allows great control of variables commonly encountered in compressor design.

3.3 Comparison of One-Dimensional Results

Only when the behaviour of the two 1-D models is compared, can an objective statement about the validity of the results of the present study be made. Table 3.3 shows three important properties at each of the points indicated in Figure 3.1.

From Table 3.3 it can be seen that the Dixon model agrees moderately well with the design done using CENCOM. At the compressor inlet a difference in static pressure of 3.30% is seen where the CENCOM model is taken to be the baseline for all percentage difference calculations. At the compressor outlet this value is 4.94%. The highest Mach number calculated by the Dixon model is 0.9993 and occurs at the impeller outlet. CENCOM reports a value of 0.9522 for this property. The total temperature at the impeller outlet is slightly lower when calculated with the Dixon model.It predicts a temperature of 436 K whereas CENCOM calculates 439 K.

Table 3.3: Comparison of One-Dimensional Results

Property	**Dixon**	**CENCOM**	**% diff.**
$p_1 \times 10^3$	92.11	95.3	3.30
T_1	285.12	287.88	0.96
c_1	12.79	101.49	-23.94
$p_2 \times 10^3$	192.3	203.7	5.59
T_2	363.80	372.31	2.29
c_2	382.07	366.12	-4.36
$p_3 \times 10^3$	218.8	217.5	-0.63
T_3	377.50	382.15	1.22
c_3	344.15	338.03	-1.81
$p_4 \times 10^3$	297.5	312.9	4.94
T_4	423.08	434.30	2.58
c_4	163.78	97.144	-68.60

CENCOM's more detailed treatment of vaneless diffuser flow is seen in the transition from the impeller to the diffuser. At the impeller outlet, the total pressure calculated by CENCOM (364.52 kPa) slightly exceeds that calculated by the Dixon model (363.55 kPa). At the diffuser inlet, however, the total pressure calculated by the Dixon model (363.55 kPa) exceeds that of CENCOM (353.37 kPa).

Nearly all differences can be attributed to differences in geometry (see Table 3.4). The Dixon model calculates the outlet diameter of the impeller, as well as the hub and shroud diameters at the impeller inlet from the design mass flow rate and rotational speed. It can also calculate the diffuser inlet and outlet diameters. Due to geometry constraints, however, the diffuser outlet diameter was set to a specific value in the present study. CENCOM accepts these various dimensions as inputs (Luiten, 2015). The larger impeller diameter leads to a higher tip speed and larger Mach number. A radially shorter diffuser has less time to extract energy from the fluid. This explains the lower outlet static pressure of the diffuser.

Table 3.4: Difference of Geometric Properties

Property	**Dixon**	**Luiten**
Impeller Outlet Diameter	0.166	0.164
Inlet Hub Diameter	0.039	0.041
Inlet Shroud Diameter	0.083	0.093

The pressure difference at the diffuser outlet cannot attributed merely to

geometry effects. Adjusting the maximum diffuser outlet diameter to compensate for the larger impeller disk diameter of the Dixon model only reduces the static pressure difference by 0.5%. With an outlet diameter of 175 mm the Dixon model matches the CENCOM model's diffuser outlet static pressure. This indicates that insufficient provision to account for the flow turning effect is made in the Dixon model.

Chapter 4

Three-Dimensional (3-D) Fluid Mechanical Modelling

4.1 Background

The initial compressor design and 3-D flow modelling was done by Luiten (2015). He created a functional and accurate flow model of the impeller. Mesh size and quality, fluid and flow models, boundary conditions and solver control were all discussed in his study.

The present study presents a review of the work done by Luiten (2015). The model he set up is analysed in detail. Where necessary it is used to answer specific questions, and study flow behaviour through the compressor.

All the boundaries as used in the current study are shown in Figure 4.1. Familiarity with the different boundaries will make the subsequent discussion easier to understand.

The different boundaries grouped according to their colour are:

- Shown in **red** are the blade surfaces. These are the full impeller blade, the impeller's splitter blade and the diffuser blade.
- **Blue** shows hub surfaces of both the impeller and the diffuser.
- Periodic boundaries for the two domains are shown in **yellow**.
- The interface between the two domains is **green**.
- The plane that corresponds to the exact impeller inlet as well as the surface at the diffuser outlet are shown in **grey**.
- For ease of viewing the shroud surfaces are left transparent.

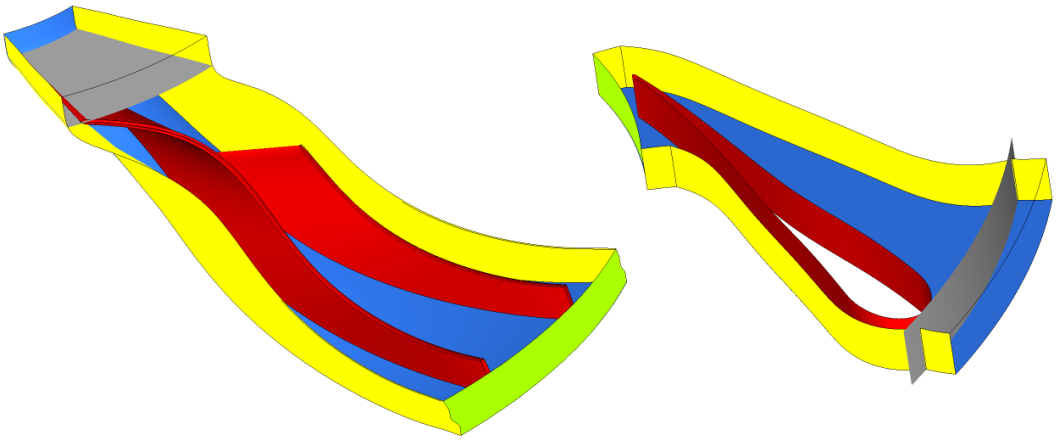

Figure 4.1: Domain Boundaries

4.2 Software

Various ANSYS programs were used to create the mesh and analyse the compressor's performance in 3-D. The most work was, however, done in CFX 18.2 (and CFX 19.1). This software packages consists of four programs: TurboGrid, CFX-Pre, CFX-Solver Manager and CFD-Post.

TurboGrid is the meshing utility used by Luiten (2015) to create an accurate mesh. CFX-Pre is used to define boundary conditions and fluid properties. CFX-Solver Manager is used locally to solve only the coarsely meshed case. Its command line utility is used to solve the finely meshed case on the high performance cluster of the University of Stellenbosch (Rhasatsha): http://www.sun.ac.za/hpc. CFD-Post is used for data extraction, solution analysis and processing of results.

4.3 Theoretical Review

The fluid model used in both domains is "Air Ideal Gas." This material is included as standard in ANSYS' "General Material" library where it is defined as per equation 4.3.1. Equation 4.3.1 introduces the molecular weight, M, and the universal gas constant, R_O. For dry air these have values of 28.97 kg/kmol and 8.31447 kJ/kmol·K respectively (Çengel and Boles, 2011).

$$\rho = \frac{Mp_{abs}}{R_O T}, dh = c_p dT, c_p = c_p(T) \tag{4.3.1}$$

The option to use the standard Redlich-Kwong model exists (ANSYS Inc., 2018*a*). The lowest temperature in the compressor is 2.1 times greater than the

critical temperature of air (132.5 K). The maximum pressure is also an order of magnitude smaller than the critical pressure (3.77 MPa) (Çengel and Boles, 2011). Hence use of the "Air Ideal Gas" model is justified and dramatically reduced computation time can be expected (Aungier, 2000).

The simulation further uses a total energy heat transfer model and the k-omega (k-ω) turbulence model. Buoyancy is not modelled.

The impeller inlet is a boundary of type "inlet." The flow direction is normal to the boundary with a total pressure of 0 kPa relative to atmosphere. The gas temperature at inlet is 287 K. This corresponds to temperatures typically seen in the turbine test cell at the onset of testing (Zhang, 2016). The exit of the diffuser is represented by a "outlet" boundary. This boundary has a pressure relative to atmosphere of 228 kPa and a temperature of 440 K. These values are informed by the 1-D model.

To describe the motion of the impeller, this domain is set to rotate at 46 000 rpm in a counter-clockwise direction. The diffuser domain, on the other hand, is stationary.

Impeller blades, splitter blades, diffuser blades and all hub and shroud surfaces are set to be smooth, no-slip, adiabatic walls. They are stationary within their domain. The only exception to this is the impeller's shroud. This wall boundary has a "counter-rotating" velocity. Hence it is stationary according to a global reference.

For the fine mesh sufficient mesh quality was shown (Luiten, 2015). Only for mesh expansion a percentage of "bad" cells was recorded. These bad cells make up 0.0227% of the total mesh and are found at the tips of both impeller and splitter blades (Luiten, 2015). Storer and Cumpsty (1991) (cited in Shum *et al.* (2000)) have shown that the static pressure at the impeller tip can be predicted accurately with a relatively coarse mesh. Hence the small region of bad cells is accepted.

Mesh dependency was also studied (Luiten, 2015). With regards to the total-to-static pressure ratio the coarse and medium meshes differed 2.45% and 2.11% from the fine mesh respectively. Efficiencies differed 2.57% and 0.11% from that calculated for the fine mesh (Luiten, 2015). For review purposes these difference are acceptable.

4.4 The Effect of Turbulence Models

Luiten (2015) used the k-ω turbulence model. The k-ω SST model, however, improves the accuracy of flow calculations for flow involving adverse

pressure gradients and is recommended for aerodynamic applications (Menter, 1994). The k-ω model was chosen regardless, because "the SST k-ω turbulence model behaved unstable and predicted unrealistic recirculation in the diffuser" (Luiten, 2015). This statement is investigated by means of a numerical experiment. The different turbulence models evaluated are:

- The Spalart-Allmaras (SA) model
- The Eddy Viscosity Transport (EVT) Equation
- The k-ω model
- The k-ω shear stress transport (SST) model

4.4.1 Coarse Mesh Properties

The coarse mesh has 577 740 elements and 629 746 nodes. All fluid models and boundary conditions as described in section 4.3 are used with the coarse mesh as well. The only exception is the turbulence model which was changed manually to study the effect of different turbulence models on outlet pressure and mass flow rate.

The coarse mesh has a y^+ distribution as shown in Figure 4.2. The y^+ contour as calculated with each turbulence model is shown. For all turbulence models the minimum value is close to zero. The mean y^+ value in the impeller is 10.01 for the k-*omega* model, 9.68 for the k-ω SST model, 10.88 for the SA model and 12.32 for the EVT model. The largest y^+ is seen at the splitter blade trailing edge.

Different turbulence models have different y^+ requirements to ensure accurate near-wall treatment. The ω-based models (k-ω and k-ω SST) require a y^+ of less than 2 for a strict low-Reynolds number implementation near the wall. Because this condition is almost impossible to achieve for most applications, CFX uses an "automatic" wall treatment for all ω-based models that allows gradual switching between wall function and low-Reynolds number grids without a loss in accuracy (ANSYS Inc., 2018*a*).

For the Spalart-Allmaras and EVT equation models the large maximum values for y^+ are troubling, because they lie outside of the range in which the viscous layer is resolved ($y^+ \approx 1$). The close agreement between the SA and k-ω SST models seen in Figure 4.3, however, indicates that, at the impeller tip, pressure can be accurately predicted with a relatively coarse mesh (Shum *et al.*, 2000).

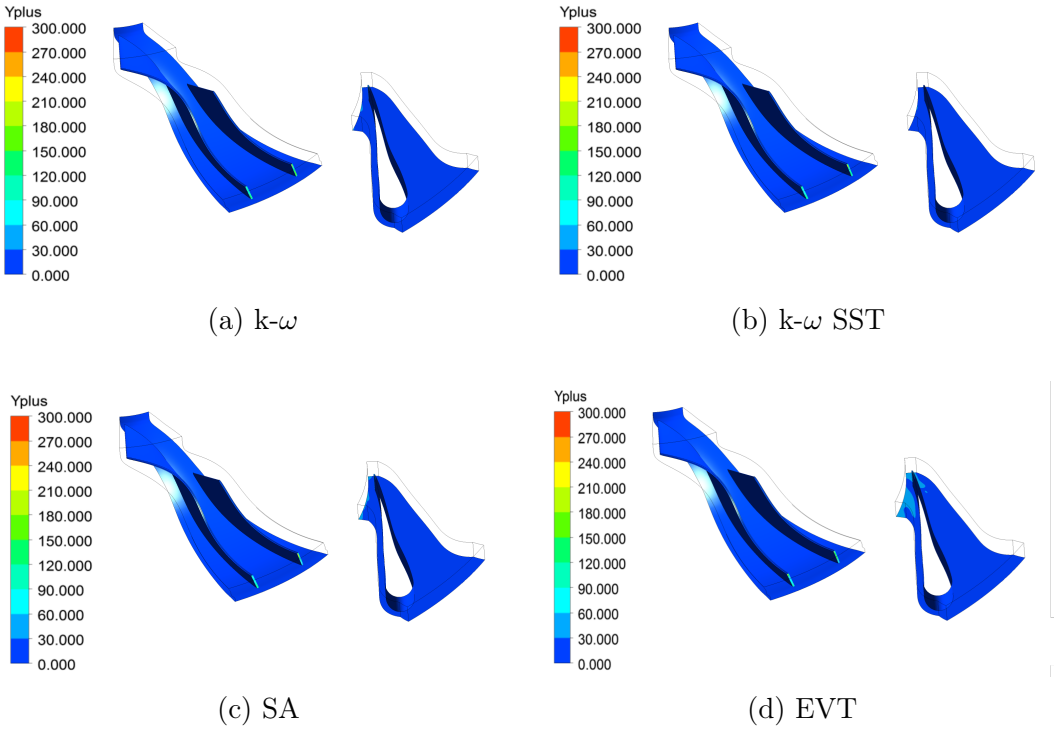

(a) k-ω (b) k-ω SST

(c) SA (d) EVT

Figure 4.2: y^+ contours for different turbulence models

4.4.2 Comparison of Turbulence Models

Using the coarse mesh, compressor curves for different turbulence models are calculated. These curves are generated by increasing the pressure and temperature values of the outlet boundary iteratively. The pressure ratio and the mass flow rate through the compressor (Figure 4.3) are recorded for every step. The rotational speed is kept at 46 000 rpm throughout.

Three of the four models are in close agreement. The EVT equation, however, is an outlier. This model reacts far more aggressively to changes in backpressure. It calculates a comparatively early onset of surge and hence a lower maximum pressure ratio (2.995). Before surging the mass flow rate is almost constant with an average of 0.6062 kg/s. Such behaviour likely occurs because neglecting the velocity divergence term in equation 2.5.2 is "strictly correct only for incompressible fluids" (ANSYS Inc., 2018*b*). Use of the EVT equation shows that unsuitable turbulence models affect results significantly.

The other three models all predict a later onset of surge and subsequently higher pressure ratios. The highest pressure ratio is 3.291 and it is calculated with the k-ω model for a mass flow rate of 0.5441 kg/s. This mass flow rate is 9.32% below the design mass flow rate. Similar behaviour, however, is seen for the SST and the SA models. They predict the greatest pressure ratio — 3.227 and 3.168 respectively — at mass flow rates of 0.4967 kg/s and 0.5088 kg/s.

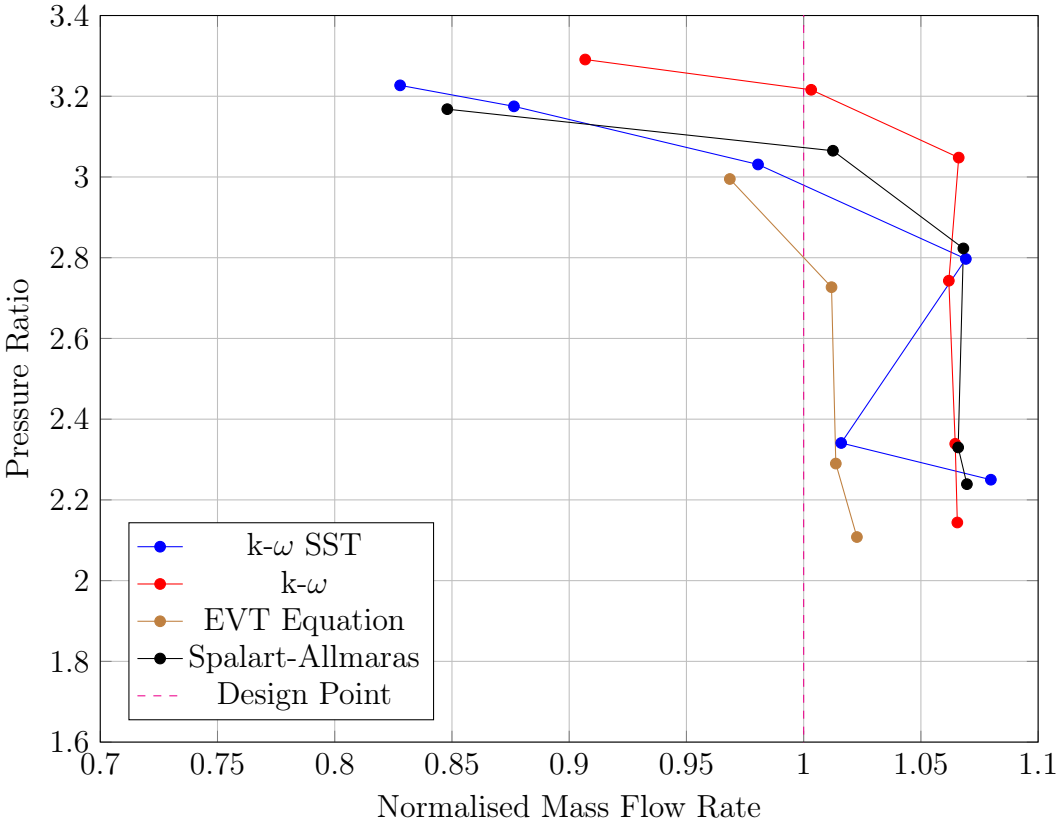

Figure 4.3: Comparison of Turbulence Models

With regards to the maximum pressure ratio calculated the models differ 1.94% and 3.74% respectively from that calculated with the k-ω model.

At the design mass flow rate, the k-ω model predicts a pressure ratio of 3.216. This is 5.75% greater than the pressure ratio calculated using the SST model at design conditions and 4.70% greater than that calculated with the SA model. The latter two models differ 1.11% from one another at design mass flow rate. This confirms the assertion of Luiten (2015) that the k-ω model over-predicts the pressure ratio.

The benefit of improved stability is only seen in the choke region. There both the SA and SST models fluctuate with regards to calculated mass flow. The k-ω model on the other hand calculates mass flow rate and pressure ratio almost linearly for increasing back pressures. Because the compressor will not operate in this region, flow behaviour seen in this region is not considered significant.

4.5 Practical Review

To assess the understanding and interpretation of Luiten's model, it was decided to replicate his analysis. Using the fine mesh created by Luiten, the present study assesses compressor performance under conditions as described in section 4.3. This analysis is compared to the previous analysis (Luiten, 2015), the CENCOM mean-line analysis of Chapter 3 and an analysis performed with the coarse mesh of section 4.4. The coarse mesh uses boundary conditions and fluid models identical to those of section 4.3 (Table 4.1).

Table 4.1: 3-D Design Results

	Fine Mesh	**Luiten (2015)**	**CEN-COM**	**Coarse Mesh**
p_1	97 780	96 690	95 250	98 340
T_1	284.60	283.30	287.88	285.50
c_1	167.10	175.10	101.49	170.80
$\dot{m}_1$	0.05	0.05	0.05	0.05
p_2	215 700	214 800	203 650	204 000
T_2	373.80	363.10	372.31	395.00
c_2	297.50	305.90	366.12	155.90
p_3	214 000	212 600	217 460	207 600
T_3	379.20	365.80	382.15	384.40
c_3	317.90	321.60	338.03	297.50
p_4	328 700	328 600	312 920	312 900
T_4	432.90	423.90	434.30	433.20
c_4	60.34	62.62	97.144	66.97
$\dot{m}_4$	-0.03	-0.03	-0.03	-0.03

The two finely meshed models (columns "Fine Mesh" and "Luiten (2015)" in Table 4.1) agree well. The biggest difference between the two is seen with regards to the inlet mass flow. This differs by 5.47%. A likely cause for this is solution history with the initial values used by Luiten (2015) being better developed than those of the present study. When the static pressures at the compressor inlet are compared the difference between the current study and that of Luiten (2015) is 1.13%. At the diffuser outlet, static temperature and absolute velocity differ by -2.12% and 3.64% respectively.

The difference for the inlet static pressure as calculated with the finely meshed model is -2.66% when compared to the 1-D model. The comparison of absolute velocity predicted by the simulation, to the results of the 1-D model is far less favourable. The 3-D model of the present study predicts a diffuser

outlet velocity that is 37.89% smaller than that calculated using the CENCOM design code. Highly three-dimensional flow in the impeller and the effects of this on velocity contribute to the discrepancy. Throughout the compressor differences between the 1-D and 3-D analysis with regards to velocity are significant.

In Table 4.1 data for a coarsely meshed model is also shown. Compared to the finely meshed model of the present study, the coarse mesh under-predicts velocity behaviour throughout the compressor. Appendix G illustrates a possible reason for this. The coarse mesh predicts more vorticity on the suction side of the main blade. Pressure calculations are, however, accurate. Considering that, by element count, the coarse mesh is 97% percent smaller than the fine mesh, a difference in outlet pressure of 4.81% is acceptable.

Chapter 5

Structural Analysis

The Rover 1S/60's impeller, turbine rotor and pinion gear are mounted to a single shaft which is held by an axial contact bearing near the pinion gear and a roller bearing between the impeller and the turbine rotor (Rover Gas Turbines Limited). From a mechanical point of view this makes it a fairly simple system. Due to the high rotational speed at the operating point, however, forces caused by the assembly's motion need to be considered. Of particular concern is the effect these will have on the tight tolerances necessary for the impeller to function effectively.

5.1 Software

The virtual impeller model was created in Autodesk Inventor Professional 2018. The model created by Luiten (2015) was imported into the workspace and manipulated using the program's extensive modelling capabilities. It was then saved as a .STP file which could be imported into ANSYS SpaceClaim without loss of detail.

The different solution methodologies were defined using ANSYS workbench. From this environment ANSYS Mechanical was called to perform pre- and post-processing. Computations were performed using the University of Stellenbosch's HPC1 (Rhasatsha): http://www.sun.ac.za/hpc.

5.2 Pre-Processing

Before accurate results can be obtained, a sufficiently accurate model must first be created. This model must reflect physical behaviour accurately by using a representative geometry, accurate material models, a mesh which does not influence results and appropriate input parameters.

5.2.1 Geometry

The geometry of the impeller is complex in that it contains both thin and thick regions, as well as edges where stress concentrations can arise. One of these edges is the edge formed where a blade meets the hub. Here stress concentrations distort calculated equivalent stresses. A fillet on the edge not only eliminates the stress concentration effect, but also allows easier machining. Furthermore it provides a curve in which a fine mesh can be created (according to parameters discussed in section 5.2.3).

A second such edge is seen in the hole through the impeller at the widest diameter of the conical section. This circumference lies on the plane of the impeller disk and is hence subject to large, radial loads. This leads to increased stresses in the area which are further aggravated by the edge. To address this a large-radius fillet is used in the region. It is in this region that the greatest stresses are calculated.

Another critical, geometric property is the shape of the impeller disk. It is slightly conical toward the turbine side with a large fillet to the rear protrusion (see Figure 6.7). This evenly distributes stresses away from the region of maximum stress.

5.2.2 Material Properties

The structural model uses a custom material defined with ANSYS' Engineering Data editor. Aluminium 7075-T6 and Aluminium 6082-T8 have properties as shown in Table 5.1 (Non Ferrous Metal Works, 2018*b*):

Table 5.1: Properties of Aluminium

Property	**Units**	**Al 7075**	**Al 6082**
Density	[kg/m^3]	2800	2700
Coefficient of thermal expansion	[1/°C]	2.35×10^{-6}	2.40×10^{-6}
Young's Modulus	[GPa]	72	70
Poisson's Ratio (AZoMaterials, 2005)	[-]	0.34	0.34
Tensile Yield Strength	[MPa]	480	255
Tensile Ultimate Strength	[MPa]	540	310

Knowledge of Young's modulus and Poisson's ratio for the material allows derivation of the bulk and shear moduli. For Aluminium 7075 they are 75 GPa and 26.87 GPa respectively. For Aluminium 6082 they likewise are 72.92 GPa and 26.12 GPa.

5.2.2.1 Over-Speed Modelling & Material Selection

Due to problems encountered when sourcing material for manufacture, Aluminium 6082 was considered. A series of over-speed analyses revealed, however, that the weaker material was not suited for the envisioned application. Table 5.2 shows that the material would have yielded near 10% over-speed. At this loading condition calculated stresses are only 0.4% below material yield strength for the strongest temper of Aluminium 6082 (Non Ferrous Metal Works, 2018*a*). This margin is unacceptable and a stronger material is chosen. All over-speed simulations were performed using the fine structural mesh.

Table 5.2: Over-Speed Results for Aluminium 6082

Property	**Units**	**46000rpm**	**48300rpm**	**50600rpm**
max. def. R	[m]	8.72×10^{-5}	9.61×10^{-5}	1.05×10^{-4}
max. def. Z	[m]	2.36×10^{-4}	2.60×10^{-4}	2.85×10^{-4}
max. total def.	[m]	2.47×10^{-4}	2.72×10^{-4}	2.99×10^{-4}
max. equiv. stress	[MPa]	210	232	254

Compare this to an impeller made from Aluminium 7075 when subjected to over-speed loading. It shows behaviour summarized in Table 5.3.

Table 5.3: Over-Speed Results for Aluminium 7075

Property	**Units**	**46000rpm**	**48300rpm**	**50600rpm**
max. def. R	[m]	8.79×10^{-5}	9.69×10^{-5}	1.06×10^{-4}
max. def. Z	[m]	2.38×10^{-4}	2.62×10^{-4}	2.87×10^{-4}
max. total def.	[m]	2.49×10^{-4}	2.75×10^{-4}	3.02×10^{-4}
max. equiv. stress	[MPa]	218	240	264

Aluminium 7075 is the superior material for this application. Even at 10% over-speed the material is 1.81 times below its yield strength. Note too that the maximum axial deflection under these conditions is still within the 1-D mean-line design tip gap clearance (by a factor of 1.32). Even at 110% design speed the impeller is unlikely to make contact with the shroud.

5.2.3 Mesh Properties

To show mesh independence of the results for the real geometry, the mesh resolution was increased using ANSYS' "coarse," "medium" and "fine" span angle center settings. The element and node counts for the respective configurations are shown in Table 5.4. Nowhere does the difference exceed one percent, except for the maximum equivalent stress. The medium mesh computes this value as being 1.03% smaller than when computed using the fine mesh (245 MPa).

This is considered sufficiently small, in part due to the fact that the medium and coarse mesh are 71% and 85.5% smaller than the fine one.

The mesh size was was defined using the "curvature" type size function. This size function computes element sizes of faces and edges such that they do not exceed "maximum size" or "curvature normal angle" settings (ANSYS Inc., 2018*c*). For the fine mesh a maximum tetrahedron size of 1.2164×10^{-2} m and a curvature angle of 18° were used. The minimum size used was 6.082×10^{-5} m.

The "curvature" size function also has the advantage that it generates a finer mesh than the "proximity" and "automatic" functions, especially in areas where the geometry is curved. Blade roots, leading and trailing edges, and critical fillets were meshed finely. These regions correspond with where stress concentration, and subsequently high stress, is expected to occur.

5.2.4 Boundary Conditions

Two boundary conditions were used. At the front of the impeller a displacement condition was used which set movement in all global coordinates to zero. A rotational velocity boundary was used on the whole part. This boundary has a value of -46 000 rpm. The direction is of limited importance due to the fact that fluid-structure interaction is not modelled. For the sake of consistency the rotational direction was chosen to match that used for the fluid mechanical analysis.

5.3 Validation of Structural Model

The technology to test the impeller's behaviour at operating speed does not exist in South Africa. The only spin facility in the country can achieve a maximum speed of 40 000 rpm (Meyer, 2018). To determine whether the structural analysis is accurate another approach is needed.

If the discretised model can be shown to be realistic for a load case, it can be reasonably assumed that other load cases using the same mesh and material characteristics will be accurate too. Hence a static deflection comparison will be used to determine the accuracy of the structural model.

5.3.1 Boundary Conditions

Because the rotational load discussed in section 5.2.4 can not be experimentally tested a different load needs to be tested on the same mesh. An axial force and its corresponding deflection should provide insight into the model's behaviour. A linearly ramped force up to a value of 8 kN is applied to the top-most surface of the impeller in parallel with the axis of rotation. The axial motion of the

inner edge of the balancing ring on the bottom of the impeller is set to be zero. This allows the impeller to shift inward under load, thus preventing localised stresses. The top-most inner edge of the hole is only permitted to move in the axial direction to prevent rigid body motion.

5.3.2 Experimental Set-Up

A simple compression test will be used to validate the numerical analysis. The compression test is performed with an MTS Criterion Model 44 Electromechanical Universal Test System. The impeller is mounted between the machine's flat grips with its balance ring resting on a fitted steel hoop. It is then compressed at a rate of 1.5 mm/min until the force gauge reads 8 kN. The motion of the cross-head and the load recorded by the load cell are measured while the experiment takes place. With a modulus of elasticity 2.7 times greater than that of the impeller the deflection of the stainless steel components (cross-head, grips and upright beams) was assumed to be negligible.

5.3.3 Results - Validation

After applying the load set discussed in subsection 5.3.1, deflection behaviour as shown in Figure 5.1 was calculated. The greatest deflection of the impeller in the axial direction has a value of 2.261×10^{-4} m which is comparable to the maximum deflection calculated with a rotating load (see section 5.4).

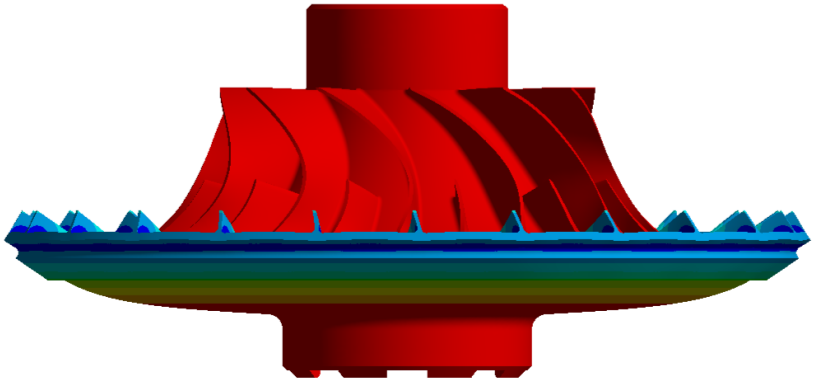

Figure 5.1: Validation Case Deflection

Stresses are distributed as shown in Figure 5.2. The maximum stress of 277 MPa is within the yield limit of the material by a factor of 1.73. The maximum stress is compressive and occurs on the shroud-side edge of the impeller blades. The effect of the blades as stress concentrators on the disk at the maximum diameter can also be seen in Figure 5.2. Careful analysis reveals small regions of heightened stress on the leading edge of the splitter blade near the root.

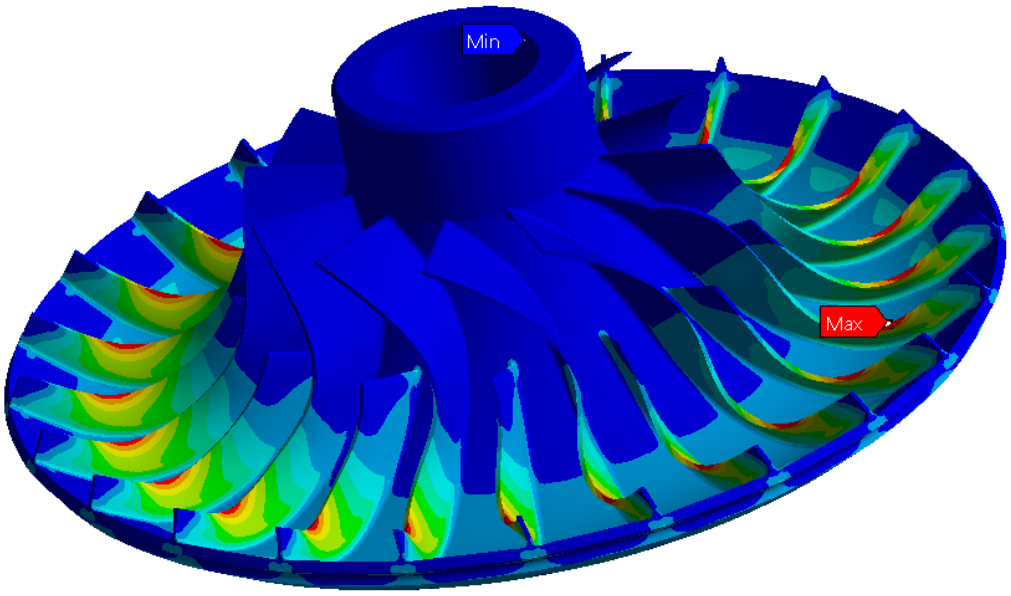

Figure 5.2: Validation Case Stress

The deflection at a known load is now compared to the experimental results. These are shown in Figure 5.3 as "Experiment." The deflection calculated using FEM is shown as "FEM." A large discrepancy is observed between simulated and measure deflections. However, the deflection of the support ring must be accounted for too. It compresses under load as indicated by the "Support" line in Figure 5.3.

To isolate the measured deflection of only the impeller, the support's deflection is subtracted from that of the impeller. the result is shown as line "Δ." This deflection is consistently 60% less than the calculated deflection.

The deflection recorded for the support can be adjusted to account for a difference in the surface area that makes contact with the grips. The supporting ring's geometry is presented in Appendix E. When the ring is pressed between the flat grips force is only applied to the 3 mm wide lip. When the impeller is inserted between the top grip and the supporting ring, the area of the ring that experiences the force is bounded by the outer edge of the impeller's balance ring and the inner edge of the supporting ring. In the linear elastic region deflection is directly proportional to stress which in turn is a function of force and area. Hence, the same force applied over a smaller area will result in greater deflections. When the deflection of the supporting ring is adjusted to account for the smaller contact area and the result is now subtracted from the deflection measured experimentally, line "$\Delta_{adj.}$" results.

This line shows deflections that are slightly less than those calculated with

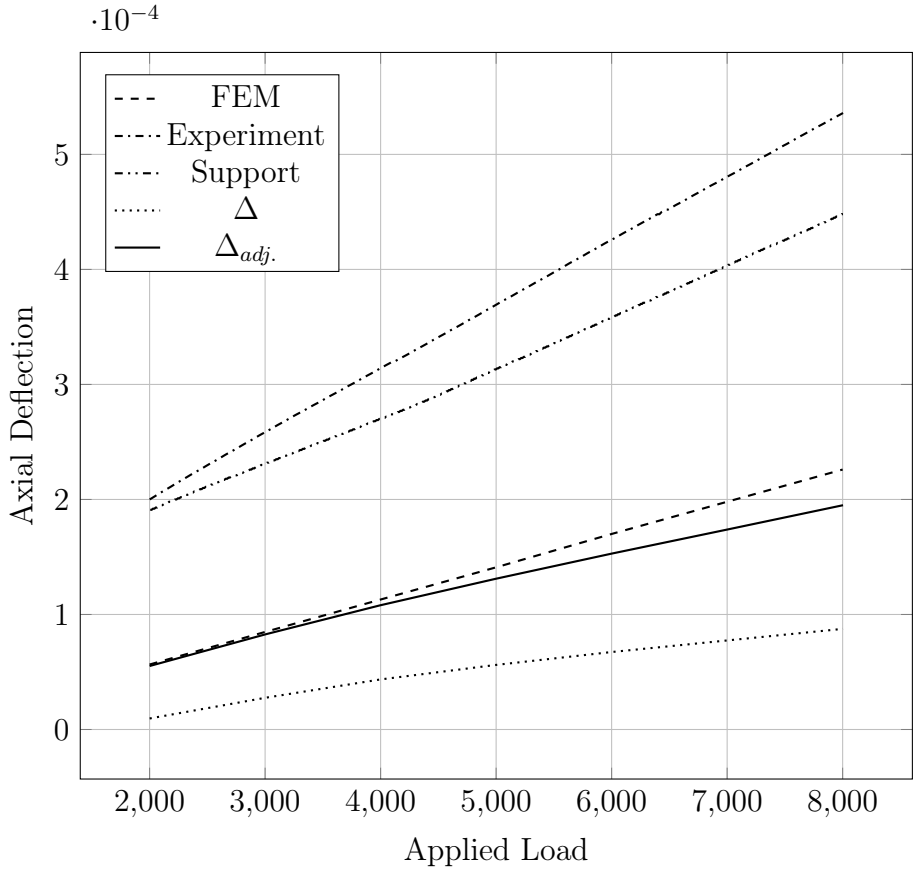

Figure 5.3: FEM Validation Results

ANSYS Mechanical. At 2 kN experimental results show a deflection that is 2% smaller than calculated. A 8 kN a maximum deflection of 195 micron is measured. This differs 14% the structural analysis as performed for the validation study.

5.4 Results - Structural

Having established that the model is a fair representation of the impeller's structural mechanics allows the calculation of part behaviour at operating conditions. The properties of greatest interest are the axial deflection and the maximum stress. Table 5.4 shows these results.

Of particular importance is the deflection in the axial direction. The deflected impeller shape can be seen in Figure 5.4. For the impeller to function as intended a narrow tip gap needs to be maintained. If, however, the deflection due to centrifugal forces exceeds the tip gap interference of blades and shroud will occur. The CompAero mean-line design uses a tip gap of 0.4 mm. The structural model predicts a maximum deflection of the blade tip of 0.238 mm

Table 5.4: Deformations and Maximum Stress for 3 Different Meshes

Property	**Units**	**Coarse**	**Medium**	**Fine**
max. def. R	[m]	8.78×10^{-5}	8.78×10^{-5}	8.79×10^{-5}
max. def. Z	[m]	2.37×10^{-4}	2.37×10^{-4}	2.38×10^{-4}
max. total def.	[m]	2.49×10^{-4}	2.49×10^{-4}	2.49×10^{-4}
max. equiv. stress	[Mpa]	212	214	218
Nodes	[-]	1 134 667	2 082 744	7 279 056
Elements	[-]	729 414	1 366 655	4 969 237

in the axial direction. With a factor for blade clearance at maximum load of 1.68 the design is accepted as safe.

The effects of thermal expansion are negligible. The temperature increases by 89.2 K in the impeller (Table 4.1). Aluminium has a coefficient of thermal expansion of 23.5×10^{-6} for temperatures between 293 K and 373 K (Non Ferrous Metal Works, 2018*b*). Thermal expansion coefficients for a variety of Aluminium alloys remain almost linear for ranges of up to 200°C (573 K) (Hidnert and Krider, 1952). At its hottest point a blade of height 5.93 mm would lengthen by 0.012 mm. This is an order of magnitude smaller than deflection due to centrifugal forces. Analysis of over-aging due to recovery temperature and its effect on the strength of the impeller, as well as heat transfer characteristics of the part are beyond the scope of the project.

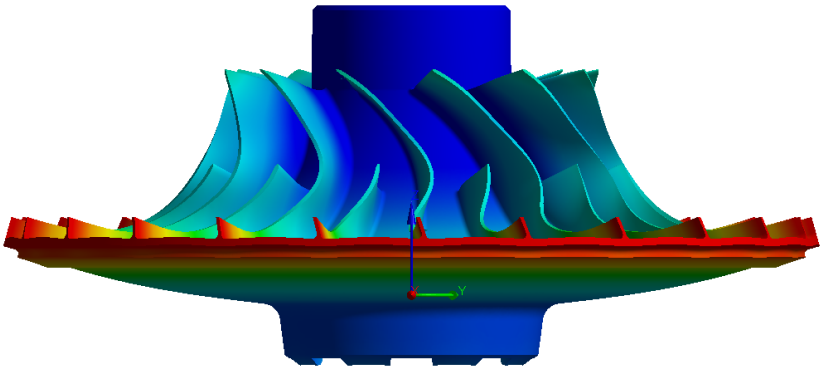

Figure 5.4: Axial Deflection of Impeller

Another important parameter is the maximum stress seen by the impeller when rotating at full speed. If the stress exceeds the yield stress of the material, permanent deformation and failure can occur. The maximum equivalent stress predicted by the structural model is 218 MPa. It occurs at the fillet in the shaft hole (see Figure 5.5). The yield stress of Aluminium 7075-T6 is 480 MPa. This is 2.20 times greater than the calculated maximum stress.

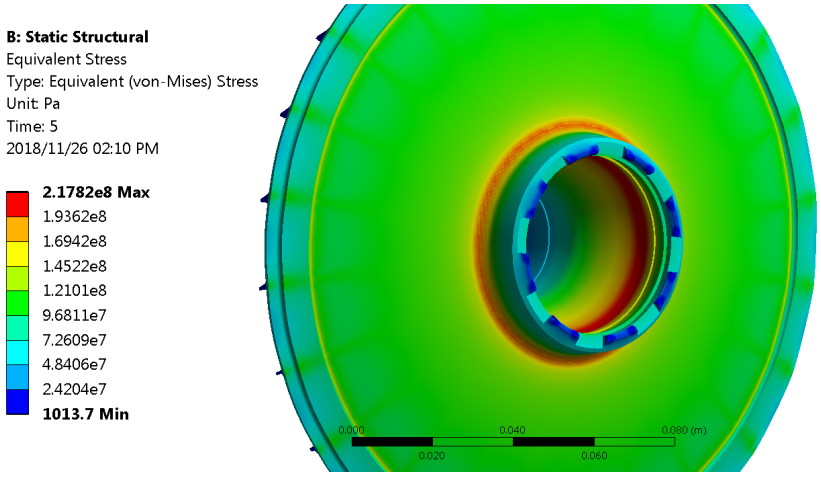

Figure 5.5: Region of Maximum Equivalent Stress

Another point of interest is the blade leading edge and the blade root near this region. Here the sharp edge leads to concentrated stresses and efforts are made to minimise such. Figure 5.6 shows the stress distribution in this area. The maximum stress that occurs here has a value of 179 MPa. Here no threat of yielding exists either.

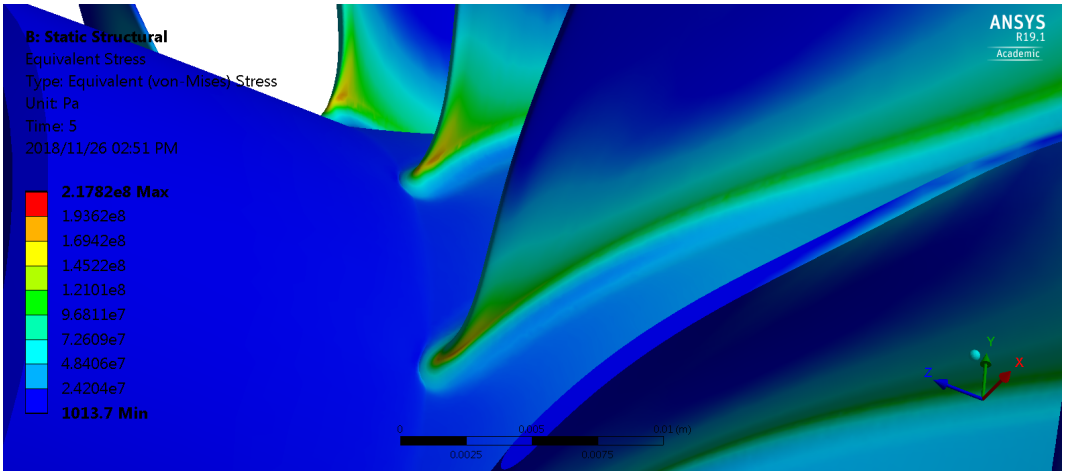

Figure 5.6: Stress Distribution at the Leading Edge

Lastly the stress distribution on the top of the impeller is considered. In Figure 5.7 it is seen that stresses are moderate throughout with slight concentrations at the blade roots. However, even here stresses are smoothly distributed and safe impeller operation is predicted.

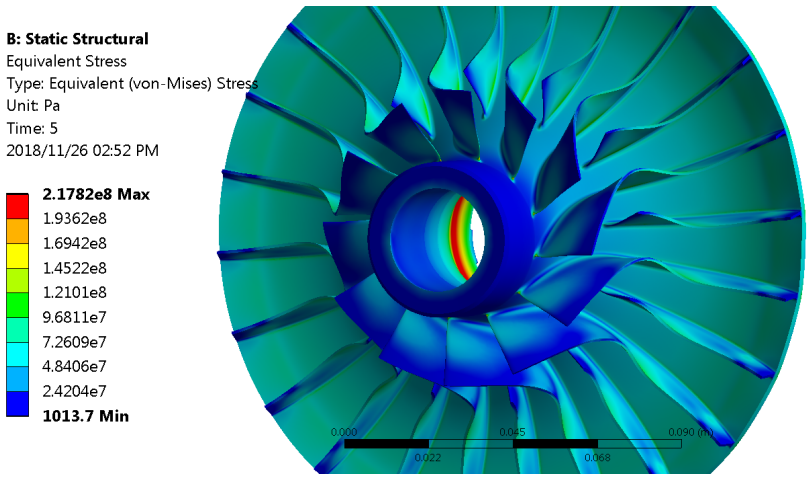

Figure 5.7: Stress Distribution on the Top of the Impeller

5.5 Results - Modal

The modal analyses were performed using the coarse and medium structural meshes (see Table 5.4 for element counts). This was done to account for the effect of mesh resolution on the modal analysis. Calculating mode shapes for a finely meshed impeller proved prohibitive and hence it is not included in the present discussion. Differences between the "coarse" and "medium" meshes are small enough that the lack of a fine mesh does not reduce the quality of results. The damped frequencies in Hertz (Hz) of the first 6 modes are shown in Table 5.5.

Table 5.5: Damped Modal Frequencies

Mode	Coarse	Medium
1	836.18	837.48
2	1 156.90	1158.31
3	1 751.68	1752.97
4	2 808.56	2800.29
5	2 810.14	2801.81
6	2 811.17	2802.90

All the modes exist above the design point speed of the impeller (766.67 Hz). The two meshes predict slightly different modes, but this is expected. The difference for the first mode is 0.16%. The greatest difference between the two meshes is 0.30% for mode number 5. The modes as calculated are independent of the resolution of the mesh.

The first mode would occur at a rotational speed of 50 249 rpm. This corresponds to 9.24% overspeed. Modes 4, 5 and 6 lie within 3 Hz of one

another. They all represent flapping of the main blade and the difference in frequency is attributed to slight variations in the mesh for individual blades. Implementing match control on the blades was prohibitive, possibly because the blade imported from TurboGrid uses a different coordinate system than the blades created from a circular pattern in Inventor (ANSYS Inc., 2018*c*). As a damped frequency of 2 800 Hz would correspond to a rotational speed of 168 000 rpm, these modes and their repetitive nature are ignored. Other mechanisms of failure will have taken effect before resonance in this region is encountered. A modal analysis of the rotating assembly — impeller, shaft and turbine rotor — was not performed.

Upon completion of the structural analysis, stresses induced in the blades due to different mechanisms are compared. Pressure differences in the fluid result in main blade stresses with a maximum magnitude of 9.2 kPa. On the splitter blade stresses of 6.0 kPa are calculated. Main blade stresses due to centrifugal forces have a maximum magnitude of 42.43 MPa. Similarly stresses of 32.67 MPa are calculated in the splitter blades. Stresses induced by centrifugal forces exceed those induced by fluid behaviour by three orders of magnitude. It is not necessary to perform a fluid-structure interaction analysis to determine the effects thereof on the strength of the part.

5.6 Axial Forces

The Rover 1S/60 has only two bearings which support the shaft. At the front (the side of the compressor) an angular contact bearing absorbs both radial and axial loading. Between the impeller and the turbine a roller bearing absorbs further radial loading.

Increasing the pressure through the compressor results in greater axial forces on the bearings. Using a 1-D analysis and fundamental pressure relations the forces acting on the front and back of the impeller and the turbine rotor respectively are calculated (see Appendix C). The sum of these needs to be absorbed by the angular contact bearing or the helical gear that transmits power from the high speed shaft to the output shaft.

The total force applied to the bearing when using the new compressor with its pressure ratio of 3.2 and the current turbine at a pressure ratio of 2.6 is 955 N. This is 2.5 times greater than the load seen by the bearing when the old compressor is used. Assuming negligible radial loads, the gas turbine should operate at 46 000 rpm for 110 hours with a reliability of 99% (see Appendix D for detailed calculations). If, however, no pressure reduction is performed and the turbine is run at the new rotor operating pressure ratio of 2.9, the load on the bearing is reduced to 856 N. Subsequently the bearing life is increased to 154 hours. Both bearing lifetimes are sufficient for “instruments and apparatus

for infrequent use" (Budynas and Nisbett, 2015). If run at 43 800 rpm to achieve only the previous compressor's operating pressure ratio of 2.6, bearing life can be extended to 1 900 hours.

5.7 Non-Destructive Testing (NDT) of the Billet

The final series of structural tests was performed once a material billet was obtained. These tests aim to ensure that no significant defects exist in the raw material which would render the material unsuited for the intended application.

The first method of NDT testing considered was by means of X-Ray. This, however, proved inconclusive due to the large size of the billet. The radiation could penetrate the billet, but a resolution at which inclusions or internal defects could be seen was not achieved.

Hence Ultrasound testing was performed on the billet. A probe with 10 mm diameter was applied perpendicularly to one of the billet's flat faces. A polycell couplant was used to facilitate the transmission of ultrasonic energy. With a probe frequency of 4 MHz "no relevant inclusions" were noted (Aziz, 2018).

Chapter 6

Design and Manufacture

6.1 Background

Mechanical behaviour and the relationship between new and existing parts have to be accounted for when designing the new compressor to ensure that the new compressor fits and functions flawlessly within the chassis of the existing gas turbine. For ease of understanding, it is useful to define the components that were designed. Parts of the existing turbine which are critical to the design process are also shown in Figure 6.1.

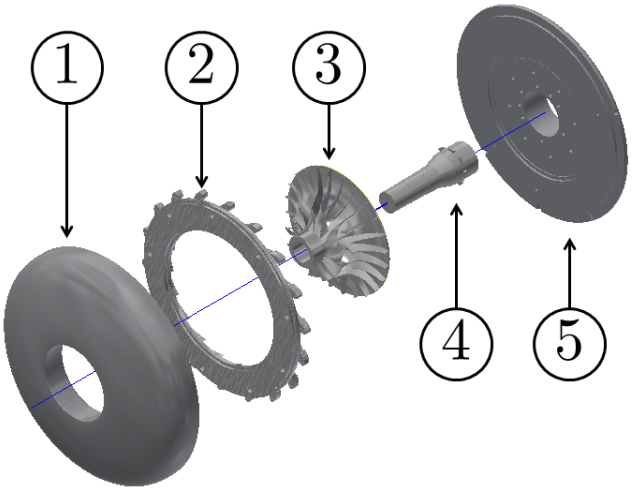

Figure 6.1: Assembly of New Parts

The different parts are:

1. Shroud
2. Diffuser
3. Impeller
4. Shaft
5. Turbine-side Disk

The shroud, shaft and turbine-side disk are all parts of the Rover 1S/60 gas turbine that need to be kept largely unchanged. These are the parts which most directly interact with the new impeller and diffuser. The other two parts — the impeller and the diffuser — will be designed and manufactured. It is important to note that the actual shroud is not shown in Figure 6.1. Shown is a place holder which represents all the dimensions critical to the design. The shroud section of the Rover IS/60 is instead a large, hollow, cast aluminium piece which is shown in Figure 6.2.

Figure 6.2: Shroud

6.2 Impeller

The impeller consists of five regions. These are illustrated in Figure 6.3.

- The front protrusion is shown in **red**.
- The **grey** hub and blades make up the flow channel.
- Shown in **yellow** is the disk.
- **Green** highlights the back protrusion.
- The hole is **black**.

Each region fulfils a different function. These need to be considered when designing the part for manufacture.

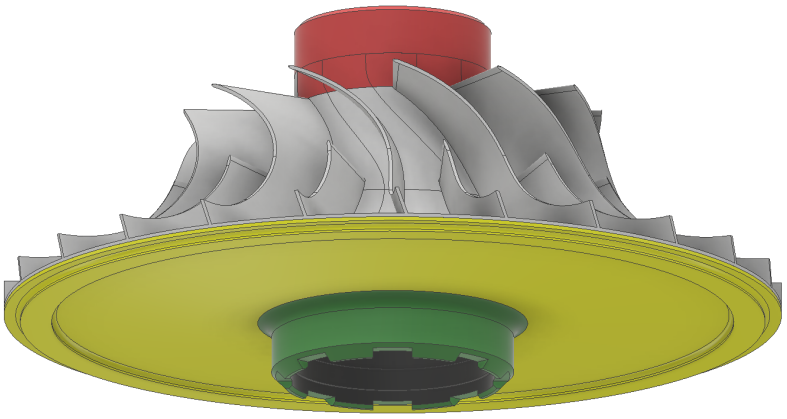

Figure 6.3: New Impeller with Regions

Because the new impeller (shown in Figure 6.3) is intended to replace the existing one, great care must be taken to ensure that it fits into the existing shroud and onto the shaft with minimal alteration to these parts. To achieve this is outer dimensions and the dimensions of the hole are matched to those of the existing impeller. Furthermore, the location of the impeller hub outlet plane relative to the existing hardware is considered. Critical dimensions obtained from existing hardware are shown in Table 6.1.

By design the blades of the new impeller are 0.5 mm shorter in the axial direction than those of the old impeller (see Table 6.1). The height of the blades is measured from the plane shown in Figure 6.4 to a plane parallel to the one shown and tangential to the main blade leading edge. To conserve the overall impeller height, this half-millimetre is added to the front protrusion.

Within the machine, the axial location of the hub outlet plane of Figure 6.4 is important. To accurately represent the fluid mechanical models discussed in chapters 3 and 4 a forward-facing radial step in the vaneless region must be avoided. In the case of the Rover 1S/60 gas turbine the hub of the diffuser

Table 6.1: Impeller Critical Dimensions

Dimension	**Old [mm]**	**New [mm]**
Inlet diameter (shroud)	93.70	87.70
Inlet diameter (hub)	41.30	41.25
Outlet/disk diameter	164.00	163.22
Front protrusion	17.60	18.34
Total height	76.70	76.70
Axial height of blades	42.80	42.25
Max. disk thickness	3.00	2.03
Protrusion diameter	50.90	50.90

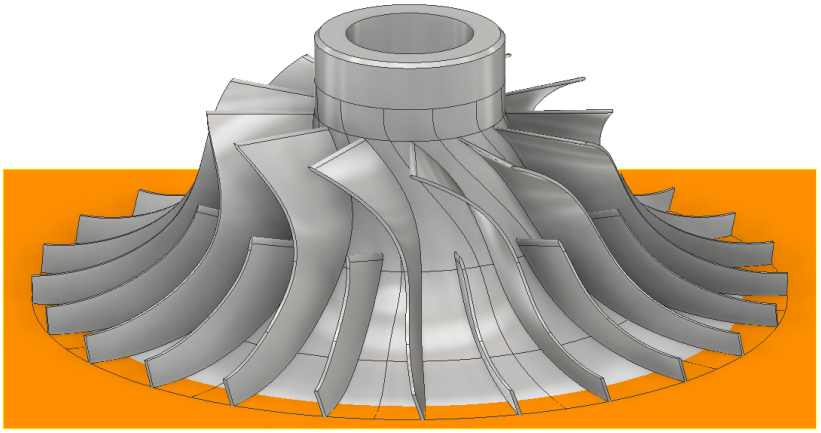

Figure 6.4: Impeller Hub Outlet Plane

is formed by the turbine side disk. The location of this part relative to the rest of the machine must remain unchanged upon installation of the modified compressor (see section 6.3). Hence the impeller's hub outlet plane needs to remain in the same location too. This is achieved by designing the axial distance from the hub outlet plane to the top of the impeller to match that of the old impeller.

A sufficient interference fit is used to install the impeller on the shaft. The old impeller fits the shaft with an interference of 0.2 mm diametrically and seats against the shaft at the locations shown in Figure 6.5. The old impeller was assembled from two parts: the rotating inlet guide vanes and the impeller. The four cylindrical faces shown in Figure 6.5 correspond to the entrance and exit of both these sub-components of the old impeller.

The new impeller is designed to interface with the shaft at all four locations. The hole through the new impeller is stepped accordingly. These steps are located such as to leave axial clearance to their counterparts on the shaft.

So doing, unwanted interference in the axial direction is prevented and it is ensured that the only axially locating interface between impeller and shaft is by means of the eight lugs at the back protrusion.

The lugs at the impeller base prevent it from twisting around the shaft and hence no torsional load needs to be absorbed by the interference fit. The pressure difference across the impeller results in an axial force of approximately 955 N. A hollow aluminium cylinder with diameters equal to those of the front protrusion of the impeller and using the same radial interference exerts a pressure of 128 MPa on a hollow steel shaft. This equates to a force of 197 kN on a section of shaft 17 mm long. This greatly exceeds the total force due to pressure acting on the impeller. Axial slipping of the impeller is unlikely.

The new impeller can be seen in Figure 6.6. The critical dimensions of the final part are also shown in Table 6.1. All outer dimensions are shown in Appendix E. For the critical diameters a close agreement between the design and the final part is seen. The axial length of the blades, the length of the front protrusion and the thickness of the disk, however, do not agree with designed measurements.

Figure 6.7 illustrates the difference between the designed and manufactured disks. The disk profile as designed is indicated by the solid line. The manufactured profile is indicated by the dashed line. The disk thickness at the balancing ring is thinner than designed. By design the balancing ring and the edge where the disk meets the back protrusion lie on the same plane. This is not the case with the final part. The balancing ring lies 0.40 mm closer to the

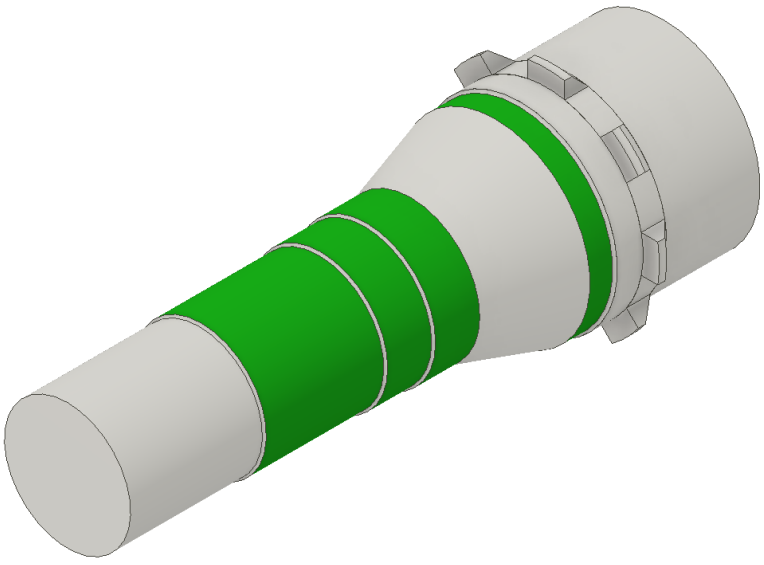

Figure 6.5: Locations where the Impeller Seats Against the Shaft

Figure 6.6: New Impeller

front of the impeller than the filleted edge. Experimental results indicate that the effect of the tapered disk on axial deflection is minimal.

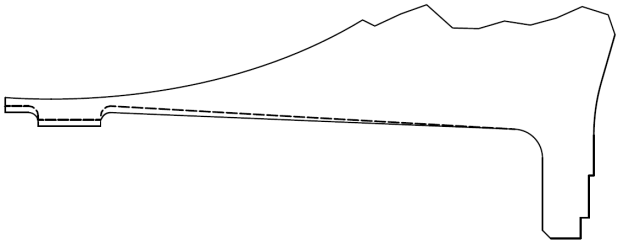

Figure 6.7: Sketch of the Altered Disk Profile

The total axial height of the blades is 0.5 mm less than designed. This was caused by by an incorrect reference condition when machining the blades. The drawing used for the turning operation of the impeller's profile and the drawing used for the 5-axis milling of the blades were not referenced to each

other correctly. This resulted in slightly shorter blades in the axial direction. One-dimensional calculations with the shorter blades predict an impeller outlet velocity of 370.21 m/s. This is an increase of 1.12% from previous calculations. The impeller outlet static pressure is reduced to 199.92 kPa – a reduction of 1.83% from the calculations of Chapter 3. The final compressor outlet static pressure is reduced by 0.50% to 311.36 kPa as a result of the reduction in impeller blade height.

The front protrusion is slightly taller than designed, however. This locates the hub outlet plane 60.59 mm from the front most face of the impeller. This is only 0.20 mm greater than the value as designed and can be adjusted as necessary during installation.

Further problems were encountered during manufacturing. When boring the hole, the vibrations of the tool caused the part to vibrate in the jaws of the mill. This resulted in the marks highlighted by the green rectangle in Figure 6.8.

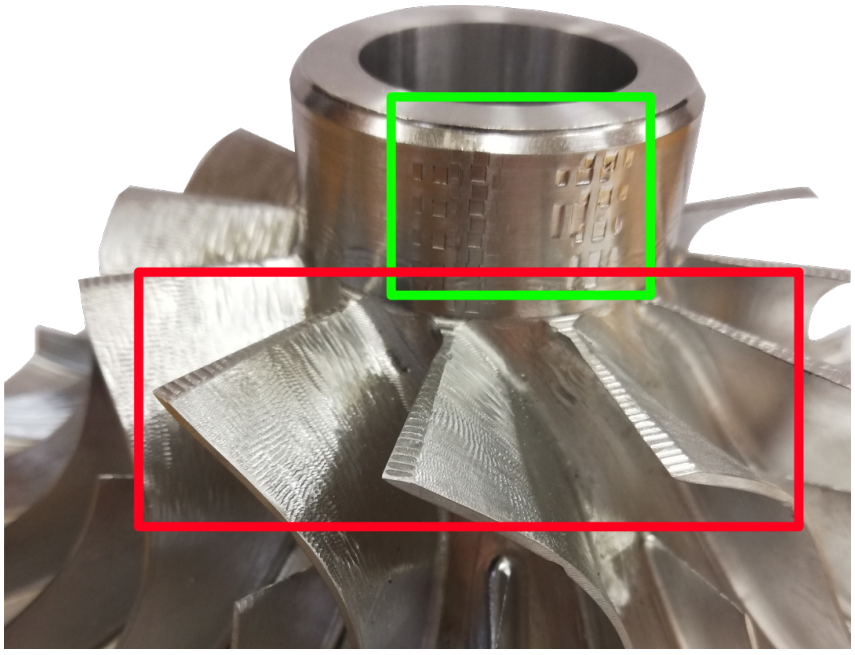

Figure 6.8: Detail of Front Protrusion

The changed leading edge (which is a result of the incorrectly referenced 5-axis milling program) is also shown in Figure 6.8. The red rectangle emphasizes the sharper leading edge. Tool marks from both the turning and cutting operations are also visible in Figure 6.8.

Despite varying from the impeller which was originally designed the new impeller can be used for experimental work. Outlet static pressure, velocity

and and temperature values are not significantly affected. Dimensions deviate from those as designed, but not so significantly as to render the part useless. The effect of poor surface finish and marring of the front protrusion will need to be observed experimentally.

6.3 Diffuser

The second part of the new compressor is the diffuser. This part is shown in Figure 6.9.

Figure 6.9: The New Diffuser

Four dimensions are important when designing the diffuser: the height from the base of the part to the hub, the inner and outer diameters of the backing ring and the maximum part diameter. The diffuser's height will ensure that the turbine side disk's location relative to the rest of the machine remains unchanged upon installation of the modified compressor. Altering the turbine side disk's location would have undesirable effects on all downstream hardware,

because much of it mounts to this part. The two ring diameters locate the diffuser in the shroud and by extension ensure radial alignment of the downstream hardware. The maximum part diameter needs to be considered when designing the diffuser, because interference with the collector is undesirable.

The new diffuser's blades are designed to be 2.8 mm shorter than those of the old impeller. Because the turbine side disk is seated against the top of the blades, it is important that the total height from the backing ring's base to the top of the blades remains the same regardless. This is achieved by thickening the backing ring.

The inner and outer diameter, together with the thickness of the backing ring, locate the diffuser in the shroud. Since the backing ring has been thickened to accommodate the shorter blades of the new design, it will now protrude above the outlet contour of the shroud. This is not problematic, because flow in this region will behave similarly to flow over a step. A small region of recirculation will form, but the majority of the flow will see a diffusing area perpendicular to the meridional which could aid in pressure recovery.

The critical dimensions of the new diffuser agree well with those of the old one. The total thickness differs most from the old design. Appendix E shows how this dimension was measured. The plane determined by this face has little structural significance and hence the difference in height is accepted. The distance between the base of the part and the hub plane as measured with the new diffuser is identical to the same dimension as measured for the old diffuser.

Table 6.2: Diffuser Critical Dimensions

Dimension	**Old [mm]**	**New [mm]**
Inner diameter	171.52	171.52
Outer diameter	248.40	248.38
Bolt locating radius	112.70	112.63
Bolt hole diameter	7.15	7.14
Height to hub	13.50	13.50
Total thickness	15.90	15.81

At a radius of 112.7 mm, distributed evenly about the axis, 9 holes of diameter 7.15 mm need to be drilled. Bolts that tie the turbine-side disk to the shroud will pass through these holes. In order to minimise disturbance of flow the holes need to be drilled through the diffuser blades. At this radius the blades are, however, exactly as wide as the holes. A small gap (0.5 mm) is hence seen in the blade surface (Figure 6.10). The gap consumes 0.83% of the

total surface area of the vane. This is small enough to assume that the effects on overall flow behaviour are negligible.

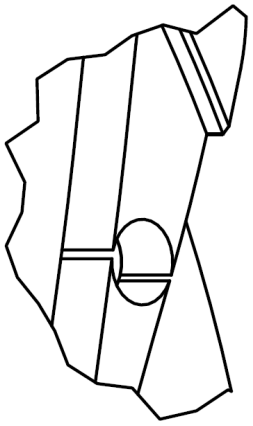

Figure 6.10: Detail of the Hole through the Diffuser Blade

6.4 Additional Considerations

From the discussion presented in sections 6.2 and 6.3 no conclusion can be drawn as to how the impeller's shroud profile relates to that of the existing shroud. This region, however, is of great importance. Clearance gap flow losses influence efficiency and pressure. Between the impeller blades and the shroud a significant risk of interference exists.

Figure 6.11 is a sketch of the impeller's shroud profile relative to the profile of the existing shroud. The gap varies from 6.5 mm at its widest to 0.96 mm at the narrowest point. Operating the compressor at these conditions would lead to significant leakage losses.

It is advisable that a shroud adapter is designed to reduce the gap between the shroud and impeller and follow the shroud profile more closely. This part should reduce the clearance gap to a value similar to that of the fluid mechanical analysis. The 1-D model assumes a tip gap of 0.4 mm. From the structural analyses it was seen that deflection of up to 0.238 mm in the axial direction can be expected. Although thermal effects and bearing deflections are assumed to be negligible it is prudent to allow for more physically realistic behaviour. Ideally then the tip gap seen for a stationary impeller at ambient conditions would be 0.5 mm.

The shroud adapter could be installed in the existing shroud by means of a shallow interference fit to the shroud's cylindrical section. Axially, the adapter could locate against the step upstream of the cylindrical section. A chamfer

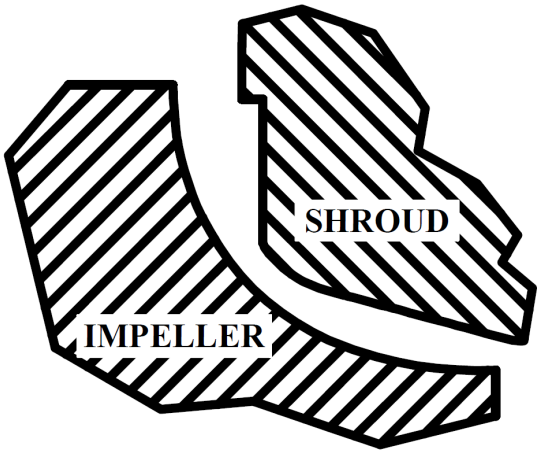

Figure 6.11: Impeller's Shroud Contour compared to Current Shroud

at the edge of this face facilitates fitting. Near the impeller outlet the shroud adapter will be held by bolts inserted through the shroud. This prevents the adapter from being pried free by the large impeller outlet pressure.

Detail design of the shroud adapter, however, is outside the scope of this project. Attention is drawn to the problem presented by the poor fit between the impeller and the existing shroud and a possible solution is recommended. The shroud adapter should be designed such as to be easily installed in the machine.

It is furthermore important to ensure that the new impeller rotates in the same direction as the old one. The diffuser also needs to be correctly located to received flow from the impeller outlet. Figure 6.12 shows that this is indeed the case. The current impeller, a drawing thereof and the drawing of the new impeller are shown side-by-side. Diffuser blades all extend radially outward in the same direction and inducer blades overlap in the same direction too.

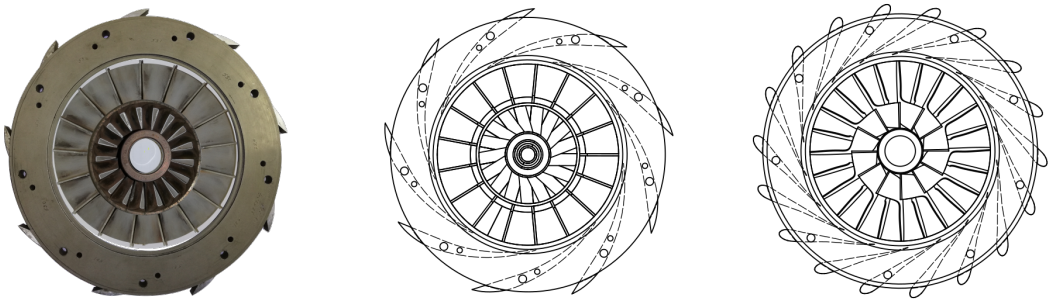

Figure 6.12: Current Compressor (left), Current Compressor Drawing (middle) & New Compressor Drawing (right)

Lastly, total axial displacement needs to be calculated. In a worst case scenario bearing tolerances, thermal expansion and deformation due to loading are compounded to produce a maximum displacement of the impeller. The sum of the worst case axial deflection, the biggest permissible tolerances for bearing diameter and race clearance (Rover Gas Turbines Limited, 1965) and the total thermal expansion at the location corresponding to the biggest axial deflection results in a maximum axial displacement of 4.054×10^{-4} m. This is 18.9% smaller than the recommended shroud gap.

Chapter 7

Conclusions & Recommendations

7.1 Conclusions

Previous fluid dynamic improvements of the compressor of an old Rover 1S/60 gas turbine calculated an increased total-to-static pressure ratio of 3.4. The unaltered compressor delivers a pressure ratio of 2.6. The efficiency of the part increased from 63.8% to 81.8% with the design presented by Luiten (2015). The present study used a 1-D analysis to determine the compressor's characteristics and found a pressure ratio of 3.2 and an efficiency of 78.6%. A recreation of the 3-D analysis calculates pressure, temperature and velocity through the compressor and deviates at most by 4.57% from the previous study. This difference is small enough in the context of a design review. It is demonstrated that the previous design meets the criteria of an increased pressure ratio and higher efficiency.

A comprehensive structural analysis demonstrates that the new impeller withstands centrifugal forces and does not operate near its natural frequencies. Over-speed modelling shows that the impeller needs to be machined from Aluminium 7075 to withstand stresses at speeds up to 110% design speed. At design speed the impeller experiences 218 MPa of stress and deflects 0.24 mm in the axial direction. This is 2.1 times smaller than the designed tip gap. Interference between the blades and the shroud is avoided. The first damped mode is calculated to occur at 837 Hz. This corresponds to a rotational speed of 50 249 rpm which exceeds the design point by 9.2%. The structural integrity of the impeller is established provided that it is operated near its design point.

The increased pressure results in a higher axial load on the angular contact bearing. The axial forces increase from 376 N to 955 N. Subsequently the bearing life is reduced to 110 hours if operating at 99% reliability with a speed of 46 000 rpm. The machine is safe to operate in the context of academic research.

Alignment of the impeller and the diffuser needs to be maintained when designing for manufacturing. Choosing a reference location and developing designs from there ensures this. By matching the outer dimensions of the new impeller and diffuser to those of the old parts easy installation is facilitated. Difficulties encountered during the manufacturing process resulted in changes to the flow channel geometry, but 1-D analysis shows that operation of the compressor is still possible. Both the impeller and diffuser are designed to be installed in the turbine in the same manner as the components they are replacing. The new parts are designed an manufactured. No existing parts were altered.

The Rover 1S/60 gas turbine with an improved compressor could be used in a solarised Brayton cycle. The higher compressor outlet pressure can possibly drive flow through a solar receiver. The present study shows that modern technology allows the modification of current and dated hardware to achieve better efficiencies and compatibility with renewable energy generation methods.

7.2 Recommendations

A CFD simulation with a set outlet pressure will often experience recirculation in the domain. A mass flow condition at the inlet can be used to prevent this. Another solution is to increase the backpressure gradually. Once the flow direction as a result of impeller rotation has been solved, the outlet pressure can be increased. The flow as calculated with the lower pressure condition is used as initial value.

Structural analysis can be streamlined by understanding which features are negligible. Fillets distribute stress and can influence the analysis. They also increase the resolution of the mesh which increases solution times.

Understanding of the analysis codes used and how their different section interact enables efficient use of the HPC. Different codes use different methods to communicate with their solvers. Issues with backward compatibility may be circumvented by understanding of the solver.

A well-developed system of record-keeping ensures that geometric parameters are tracked throughout the development cycle. Where data from other work is used, record-keeping identifies discrepancies.

A firm understanding of the manufacturing process is necessary. File formats and their interpretation by different programs can have unintended consequences. Great care must be taken to prevent features native to the software from manifesting in the physical part, particularly when using CAM.

7.3 Future Work

Keeping the overall design intent in mind makes it clear that great potential for future work related to the present project exists. Some recommended tasks are discussed below.

Firstly a series of benchmark tests using the existing compressor need to be performed. Similar work has been performed previously (Zhang, 2016), but another series of benchmark tests is needed. The fuel supply system has been changed (Marsh, 2018) and the effects of this on the current compressor need to be recorded. Benchmark testing will also create familiarity with the turbine and the test cell environment.

Once the decision is made to proceed to the installation of the new compressor certain tasks need to be performed.

- The turbine needs to be dismantled.
- The bearings need to be inspected for signs of wear and damage.
- The existing impeller and rotating inlet guide vane unit need to be removed from the shaft.
- The shaft needs to be inspected for damage.

Jigs and tooling to install the new impeller need to be manufactured. Appendix F provides examples of such tooling and instructions on how to use them. It is important that this be done in a timely manner. The availability of appropriate jigs and tools will ensure a safer and easier installation of the impeller. Likewise, the shaft needs to be prepared for the fitting of the new impeller. It may be necessary to polish out burs inflicted during disassembly.

After performing the necessary preparatory steps the impeller needs to be installed on the shaft. Quality assessment of the impeller installation needs to be performed too.

The shroud adapter needs to be designed and installed in the shroud. A quality assessment of the installation needs to be performed. Concentricity and precision of fit in the axial direction are critical during this step.

The new impeller-shaft assembly and diffuser need to be installed in the gas turbine. Ensure that the diffuser seats correctly to the shroud and that the impeller rotates freely. Then assemble the gas turbine again taking care to perform the recommended inspections as the assembly progresses.

For an initial series of tests it is recommended that the new compressor be tested only to the current pressure ratio. Calculations predict that this will occur at 43 800 rpm. Then, the combustor must be modified to account for the higher compressor outlet pressure.

Lastly, the new compressor needs to be tested to design condition. Parameters deemed important should be recorded and experimental data compared to numerical results.

List of References

ANSYS Inc. (2018*a*). Cfx-solver modeling guide. Digital Reference.

ANSYS Inc. (2018*b*). Cfx-solver theory guide. Digital Reference.

ANSYS Inc. (2018*c*). Mechanical apdl 19.1 basic analysis guide. Digital Reference.

Asif, M. and Muneer, T. (2007). Energy supply, its demand and security issues for developed and emerging economies. *Renewable and Sustainable Energy Reviews*, vol. 11, no. 7, pp. 1388–1413. ISSN 13640321.

Aungier, R.H. (ed.) (1995*a*). *Centrifugal Compressor Stage Preliminary Aerodynamic Design and Component Sizing*. Elliott Company, The American Society of Mechanical Education for Chemical Engineers.

Aungier, R.H. (1995*b*). Mean streamline aerodynamic performance analysis of centrifugal compressors. *Transactions of the ASME*.

Aungier, R.H. (2000). *Centrifugal Compressors: A Strategy for Aerodynamic Design and Analysis*. ASME Press.

Aziz, J. (2018 August). Ultrasonic inspection report: Aluminium billet. techreport, Akram Consulting.

AZoMaterials (2005 May). Aluminium - specifications, properties, classifiactions and classes. https://www.azom.com/article.aspx?ArticleID=2863.

Boyce, M.P. (2012). *Gas Turbine Engineering Handbook*. 4th edn. Butterworth-Heinemann.

Budynas, R.G. and Nisbett, J.K. (2015). *Shigley's Mechanical Engineering Design*. McGraw-Hill Higher Eduaction.

Çengel, Yunus A.; Cimbala, J.M. (2014). *Fluid Mechanics: Fundamentals and Applications*. McGraw-Hill Higher Eduaction.

Çengel, Y.A. and Boles, M.A. (2011). *Thermodynamics: An Engineering Approach*. McGraw-Hill Higher Eduaction.

Clements, W.W. and Artt, D.W. (1989). The influence of diffuser vane leading edge geometry on the performance of a centrifugal compressor. *Gas Turbine and Aeroengine Congress and Exposition*.

Cook, R.D., Malkus, D.S., Plesha, M.E. and Witt, R.J. (2002). *Concepts and Applications of Finite Element Analysis*. John Wiley & Sons.

Daily, J.W. and Nece, R.E. (1960). Chamber dimension effects on induced flow and frictional resistance of enclosed rotating disks. *Journal of Basic Engineering*.

Department of Energy (2018 November). Production and operating capacity. Online, redis.energy.co.za/power-production/.

Dixon, S.L. (2010). *Fluid Mechanics and Thermodynamics of Turbomachinery*. Sixth edn. Butterworth-Heinemann.

EPA (2017). Global Greenhouse Gas Emissions Data.
Available at: `https://www.epa.gov/ghgemissions/global-greenhouse-gas-emissions-data`

gasturbineworld (2018 January). Rover gas turbine engines. Online.
Available at: `http://www.gasturbineworld.co.uk/rovergasturbine.html`

Hidnert, P. and Krider, H.S. (1952). Thermal expansion of aluminum and some aluminum alloys. *Journal of Research of the National Bureau of Standards*.

Homann, C. (2015). *Effects of Solar Hybridization on the Performance of a Gas Turbine*. Master's thesis, Stellenbosch University.

Inman, D.J. (2014). *Engineering Vibration*. Pearson Education Limited.

Japikse, D. and Baines, N. (1989). *Diffuser Design Technology*. Concepts ETI Inc. ISBN 0-933283-08-3.

Krige, D. (2013). *Performance Evaluation of a Micro Gas Turbine Centrifugal Compressor Diffuser*. Master's thesis, Stellenbosch University.

Kröger, D.G. (2011 April). The stellenbosch university solar power thermodynamic cycle. Online.

Lieblein, S. (1959). Loss and stall analysis of compressor cascades. *Journal of Basic Engineering*.

Luiten, R.V. (2015). *Performance Improvement of the Rover 1S/60 Gas Turbine Compressor*. Master's thesis, Stellenbosch University.

Marsh, D. (2018 Novemeber). Conversion of a kerosene-fuelled gas turbine to run on propane. Personal Communication.

Menter, F.R. (1994). Two-equation eddy-viscosity turbulence models for engineering applications. *AIAA Journal*.

Meyer, G. (2018 July). Availability of spin test facility. Personal Correspondence.

NASA Earth Observatory (2010). Global Warming.
Available at: `https://earthobservatory.nasa.gov/Features/GlobalWarming/page2.php`

Non Ferrous Metal Works (2018 July*a*). Aluminium data sheet 6082. Brochure.

Non Ferrous Metal Works (2018 April*b*). Aluminium data sheet 7075. Brochure.

Philibert, C. (2011). Solar energy perspectives. Tech. Rep., International Energy Agency.

Rover Gas Turbines Limited (). Rover gas turbines. Brochure.

Rover Gas Turbines Limited (1965 April). *Rover Gas Turbines: Engines Type IS/60 & IS/90 Overhaul Manual*. Rover Gas Turbines Limited, Solihull, Warwickshire, England, 1st edn.

Saravanamuttoo, H.I.H., Cohen, H. and Rogers, G.F.C. (2001). *Gas Turbine Theory*. Pearson Education.

Sayers, A.T. (1990). *Hydraulic and Compressible Flow Turbomachines*. University of Cape Town.

Shum, Y.K.P., Tan, C.S. and Cumpsty, N.A. (2000 October). Impeller-diffuser interaction in a centrifugal compressor. *Journal of Turbomachinery*, vol. 122, pp. 777 – 786.

Spalart, P.R. and Allmaras, S.R. (1994). A one-equation turbulence model for aerodynamic flows. *La Recherche Aérospatiale*, vol. 1, pp. 5–21.

Versteeg, H.K. and Malalasekera, W. (2007). *An Introduction to Computational Fluid Dynamics: The Finite Volume Method*. 2nd edn. Pearson Education. ISBN 978-0-13-127498-3.

Zhang, Y. (2016). *Pre-Study for the Conversion of a Gas Turbine from Liquid to Gaseous Fuel*. Master's thesis, Stellenbosch University.

Appendices

Appendix A

Governing Laws

In the following sections a brief summary of the four laws that govern fluid behaviour in a turbomachine is presented. These apply to all turbomachines regardless of size and type (Dixon, 2010). Velocity relations as they relate to compressor analysis are also presented.

A.1 The Equation of Continuity

Let c be the stream velocity and A_n the area normal to the flow direction at an arbitrary location in the stream. The mass flow of a differential fluid element can be expressed as shown in equation A.1.1.

$$\frac{\mathrm{d}m}{\mathrm{d}t} = \rho c \mathrm{d}A_n \tag{A.1.1}$$

Continuity allows the designer to determine at least one property at any given point in the turbine. It is also fundamental to the error checking process.

A.2 The First Law of Thermodynamics

By this law, a system that undergoes a complete cycle of working and heating can be described by equation A.2.1. In that equation heat supplied to the system is represented by $\oint \mathrm{d}Q$. Likewise, $\oint \mathrm{d}W$ represents work done by the system.

$$\oint (\mathrm{d}Q - \mathrm{d}W) = 0 \tag{A.2.1}$$

It is, however, more practical to describe a change in the system between states 1 and 2. Now an energy change must be accounted for (equation A.2.2). Here energy, E, is the sum of the kinetic energy, $\frac{1}{2}mc^2$, the potential energy, mgz, and the internal energy, U.

$$\int_1^2 (\mathrm{d}Q - \mathrm{d}W) = E_2 - E_1 \tag{A.2.2}$$

In a steady flow, equation A.2.2 can be simplified as shown by Çengel and Boles (2011). The resultant equation can be greatly simplified by the introduction of *stagnation enthalpy*, $h_0 = h + \frac{1}{2}c^2$ and the assumption that the potential energy per unit mass in negligible. Now the energy equation can be written as in equation A.2.3.

$$\dot{Q} - \dot{W}_x = \dot{m}(h_{02} - h_{01}) \tag{A.2.3}$$

When the machine operates adiabatically, it is common practice to set $\dot{Q} = 0$ and manipulate the sign of $\dot{W}_x$ to describe whether the machine produces or absorbs work.

A.3 The Momentum Equation

This equation is a direct application of Newton's second law of motion to a system.

$$\sum F_x = \frac{\mathrm{d}}{\mathrm{d}t}(mc_x) \tag{A.3.1}$$

For turbomachines, which operate in a rotating frame of reference, it is more useful to apply equation A.3.1 in a form that accounts for the moments of forces (equation A.3.2). In that equation the axis of rotation is A-A, r is the distance from the axis to the center of mass and c_θ is a velocity component that is perpendicular to both the axis of rotation and the vector r.

$$\tau_A = m\frac{\mathrm{d}}{\mathrm{d}t}(rc_\theta) \tag{A.3.2}$$

Multiplying equation A.3.2 throughout by the angular velocity, Ω, turns it into the *Euler pump equation*. This equation describes work per unit mass.

$$\Delta W = \Omega(r_2 c_{\theta 2} - r_1 c_{\theta 1}) \tag{A.3.3}$$

The sign of the term on the left side of equation A.3.3 indicates whether one is dealing with a pump or a turbine. If ΔW is positive it is a pump. If it is negative, a turbine. Simplify as follows: $U = \Omega r$ and $\Delta h_0 = \Delta(U c_\theta)$, and assume adiabatic operating conditions to rewrite equation A.3.3 as equation A.3.4.

$$I = h_0 - U c_\theta \tag{A.3.4}$$

I is the rotational stagnation enthalpy, commonly referred to as rothalpy. It is constant along streamlines through a turbomachine (Dixon, 2010). With a little manipulation of equation A.3.4 it can be shown that the relative stagnation enthalpy is constant if the radius of a streamline passing through the machine remains constant.

A.4 The Second Law of Thermodynamics - Entropy

The second law of thermodynamics and the concept of entropy allow the formulation of a hypothetical, ideal process. For a cycle whose every process is reversible, for a finite change of state, entropy can be defined as in equation A.4.1

$$S_2 - S_1 = \int_1^2 \frac{\mathrm{d}Q_R}{T} \tag{A.4.1}$$

Accounting for irreversibilities is now as simple as adding a term on the right side of equation A.4.1. An adiabatic and reversible process will experience no change in entropy. The ideal thermodynamic process in a turbomachine is hence isentropic. An accurate metric of a machine's optimal performance can now be established.

Entropy also allows a re-formulation of the first law of thermodynamics in the absence of gravity, motion and similar effects. Equation A.4.2 shows this new formulation.

$$T\mathrm{d}s = \mathrm{d}u + p\mathrm{d}v \tag{A.4.2}$$

This form of the equation is useful, because it is wholly composed in terms of properties of the system. Another useful trait of entropy is that its value remains the same across both frames of reference. Any amount of entropy created equals "work lost" (Dixon, 2010).

Appendix B

Python Code: Dixon Model

```
import numpy as np
import matplotlib.pyplot as plt
from astropy.table import Table, Column

# DIXON MODEL
# A computer that uses the approach described in Dixon's
# "Fluid Mechanics and Thermodynamics of Turbomachinery"
# to determine flow behaviour in a compressor.
# Built by: Timmo Schommarz

# Design Requirements and Constants

P = 86.484e3    # W (Luiten, 2015)
N = 46000    # rpm
mdot = 0.6   # kg/s
T01 = 293    # K
p01 = 101.325e3   # Pa

Cp = 1005    # J/kgK
y = 1.4      #
Z = 12 + 12 * 0.7
R = 287      # J/kgK

# Determining the Blade Speed and Impeller Radius

deltaW = P/mdot
sigma = 1-0.63*np.pi/Z  # Stanitz slip factor
U2 = np.sqrt(deltaW/sigma)
r2 = U2/(N*np.pi/30)
```

```
U2 = N*np.pi/30  # rotational speed in rad/s

# Design of Impeller Inlet

a01 = np.sqrt(y*R*T01)

# f(Mrel1)
bs1 = np.linspace(10,80,1000)
Mrel = 0.7


def fMrel(Mrel1, bs1):
    return (Mrel1**3 * np.sin(np.deg2rad(bs1))**2 * \
    np.cos(np.deg2rad(bs1))) / (1 + 1/5 * Mrel1**2 * \
    np.cos(np.deg2rad(bs1))**2)**4


maxMrel = max(fMrel(Mrel,bs1))
maxbeta = np.rad2deg(np.arccos(np.sqrt(0.7 + 1.5/Mrel**2 \
    - np.sqrt((0.7 + 1.5/Mrel**2)**2 - 1/Mrel**2))))
print("maxbeta is: \t", maxbeta)

k = (N*np.pi/30)**2 * mdot / (np.pi * y * a01 * maxMrel * p01)
r_rh1rs1 = np.sqrt(1 - k)

M1 = Mrel * np.cos(np.deg2rad(maxbeta))
rho1 = (p01/R/T01)/(1 + 1/5 * M1**2)**2.5
a1 = a01/(1 + 1/5 * M1**2)**0.5
cx1 = M1 * a1
rs1 = np.sqrt(mdot/(np.pi * k * rho1 * cx1))
rh1 = rs1 * r_rh1rs1
A1 = np.pi * (rs1**2 - rh1**2)

# Design of Impeller Exit
# The impeller efficiency is assumed, based
# on the example of Dixon (2010), to be 90%.
etai = 0.90
cr2 = cx1  # Radial velocity equals axial velocity
cO2 = U2 * sigma
c2 = np.sqrt(cr2**2 + cO2**2)

alpha2 = np.rad2deg(np.arctan(cO2/cr2))  # flow angle

# Temperature ratio across the impeller
```

```
r_T02T01 = 1 + deltaW/Cp/T01

T02 = T01 * r_T02T01
r_T02sT01 = etai * (r_T02T01 - 1) + 1

# Total-to-total pressure ratio across impeller
r_p02p01 = r_T02sT01**(y/(y-1))

p02 = p01 * r_p02p01
print("p02 is:\t\t",p02)
T2 = T02 - c2**2/2/Cp
p2 = p02 * (T2/T02)**(y/(y-1))
rho2 = p2/R/T2
b2 = mdot/(2 * np.pi * rho2 * cr2 * r2) - 0.58/1e3
print("b2 is:\t\t", b2)
A2 = 2 * np.pi * r2 * b2
M2 = c2/np.sqrt(y * R * T2)

# Flow in the Vaneless Space
ratioVLD = 1.1  # Dixon (2010)
cO2d = r2 / (ratioVLD * r2) * cO2
cr2d = r2 / (ratioVLD * r2) * cr2
alpha2d = np.rad2deg(np.arccos(cr2d / cO2d))
c2d = np.sqrt(cO2d ** 2 + cr2d ** 2)
c2dnew  = 0

while abs(c2d - c2dnew) > 1e-6:
    T2d = T02 - c2d**2/2/Cp
    a2d = np.sqrt(y * R * T2d)
    M2d = c2d/a2d
    p2d = p02/(T02/T2d)**(y/(y-1))
    rho2d = p2d/R/T2d
    A2d = 2 * np.pi * ratioVLD * r2 * b2
    cr2new = mdot/(rho2d * A2d)
    c2d = c2dnew
    c2dnew = np.sqrt(cr2new**2 + cO2d**2)

print("c2 is: \t\t", c2)
print("c2dnew is:\t", c2dnew)
T02d = T2d + 0.5 * c2dnew**2 / Cp
p02d = p2d/((T2d/T02d)**(y/(y-1)))
print("p02d is: \t", p02d)
M2dfin = c2dnew/np.sqrt(y * R * T2d)
alpha2dfin = np.rad2deg(np.arctan(cO2d/cr2new))
```

```
r2d = ratioVLD*r2

# The Vaned Diffuser
# Dixon suggests that 0.875 efficiency is "close to the maximum
# efficiency for this type of diffuser." To err on the
# side of caution a efficiency of 0.85 was chosen.
etad = 0.85
r3 = 0.13225  # from geometry constraints
C_pid = 1 - 1/(r3/r2d)**4  # ideal pressure rise coefficient
C_p = C_pid*etad  # pressure rise coefficient
q2d = 0.5 * rho2d * c2dnew**2
p3 = p2d + C_p*q2d
c3 = c2dnew * (1 - C_pid)**0.5

# Determining the exit stagnation pressure, overall
# efficiency and miscellaneous properties
T3 = T02 - c3**2/2/Cp
rho3 = p3/R/T3
p03 = p3 + 1/4 * rho3 * c3**2
T03ss = T01 * (p03/p01)**((y-1)/y)
etac = Cp * T01 * (T03ss/T01 - 1)/deltaW
T1 = T01 / (1 + (y-1)/2*M1**2)
p1 = p01 * (T1/T01)**(y/(y-1))

# write flow properties to file
np.savetxt('DixonModel.csv', [[p1, p2, p2d, p3],
            [T1, T2, T2d, T3],[cx1, c2, c2d, c3]],
            fmt='%.2f', delimiter=',', header="#1, #2, #3, #4")
```

Appendix C

Axial Forces

In the following sections a discussion of calculations for the force experienced by the angular contact bearing is provided. Both the impeller and the turbine, and the forces acting on on the front and back of either are examined. The back of the rotor is taken to mean the side facing toward the nozzle of the gas turbine. The front faces toward the pinion gear. Figure C.1 shows the pressures acting in the axial direction which cause forces seen by the bearing.

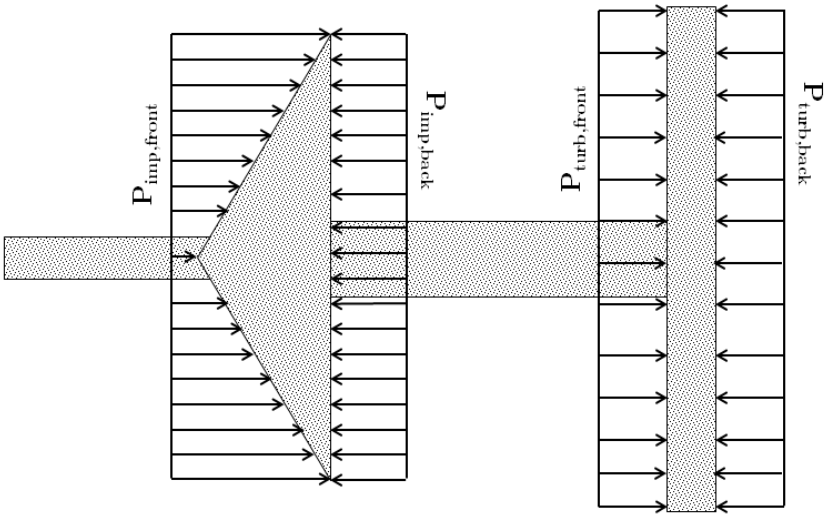

Figure C.1: Sketch of Axial Forces

C.1 Forces on the Impeller

The axial component of force acting on the front of the impeller was retrieved from ANSYS CFD-Post with a in-built function. The program calculates the approximate force using equation C.1.1 where $\overrightarrow{a}$ is the force vector specified by the user. For the present study only forces in the axial direction — the

global z-axis — are of interest. Similarly, $\overrightarrow{F_p}$ is the pressure force vector and $\overrightarrow{F_v}$ represents the viscous force vector (ANSYS Inc., 2018*b*).

$$F_1 = \overrightarrow{a}\overrightarrow{F_p} + \overrightarrow{a}\overrightarrow{F_v} \tag{C.1.1}$$

Pressure induced forces are of particular interest to the present problem. The pressure force vector is calculated as per equation C.1.2.

$$\overrightarrow{F_p} = \sum_{i=1}^{n}(p - p_{ref})A\hat{n} \tag{C.1.2}$$

The use of the relative pressure $(p - p_{ref})$ reduces the effect of numerical errors. Further variables used in equation C.1.2 are n, the number of faces, A, the area of the face and $\hat{n}$ the unit vector normal to the face (ANSYS Inc., 2018*b*).

By the method discussed above a total force acting in the axial was found: 76.26 N. This was then multiplied by 12 to give the force acting on the whole front of the impeller (not just the flow channel used for the CFD analysis). The total force acting on the front of the impeller is 915.12 N.

To calculate the force exerted on the back of the impeller the relative static pressure at the impeller tip (p_2) was multiplied by the area of the impeller's disk. It is important to use the relative pressure in order to maintain agreement with the method shown in equation C.1.2. The static pressure was taken as calculated by the Aungier model (see Chapter 3). The area was calculated as per equation C.1.3.

$$A_{imp} = \pi/4 * (d_2 - d_shaft) \tag{C.1.3}$$

The resultant force is 2 002 N. The effective force exerted on the shaft due to the impeller's pressure loading is 1 087 N.

To gain some perspective compare the axial loading of the new impeller to that of the old one. The axial force on the front of the old impeller is 596.53 N (Luiten, 2015). The force on the back is calculated as for the new impeller with pressure values as described in a previous study (Luiten, 2015) and has a value of 1 049‘N. This results in a force of 452 N on the shaft. This is 2.4 times smaller that the force exerted on the shat by the new impeller. The rise in force is a direct consequence of the increased pressure ration achieved by the new impeller.

C.2 Forces on the Turbine

In order to calculate the axial forces acting on the turbine, the pressure at the rotor inlet and at the rotor outlet need to be found. The disk area of the turbine must also be determined. To calculate the turbine mean radius the mean rotational speed is divided by the angular velocity at operating conditions. At the front of the turbine, the disk area is taken to be the mean radius' area less the area occupied by the shaft. At the back of the turbine the shaft's cross-sectional area is not subtracted, because of how the turbine attaches to the shaft.

To calculate the pressure at the inlet of the stator, the outlet pressure of the compressor is multiplied by 0.97. This simple manipulation assumes a three percent drop in total pressure through the combustor. The static compressor outlet pressures used are 312.9 kPa for the present study (from Chapter 3) and 223.9 kPa for the old compressor (Luiten, 2015).

First calculate the static temperature at the stator inlet (T_1) using equation C.2.1. Velocity and total temperature are known for the turbine (Zhang, 2016).

$$T_1 = T_{01} - \frac{c_1^2}{2 * c_p} \tag{C.2.1}$$

From that calculate the total pressure at the stator inlet (P_{01}) (equation C.2.2).

$$\frac{p_1}{p_{01}} = \left(\frac{T_1}{T_{01}}\right)^{\gamma/(\gamma-1)} \tag{C.2.2}$$

Now calculate the pressure ratio of turbine inlet to turbine outlet using equation 7.5 from Saravanamuttoo *et al.* (2001) (here replicated as equation C.2.3).

$$\Delta T_{0s} = \eta_s T_{01} \left[1 - \left(\frac{1}{p_{01}/p_{03}}\right)^{(\gamma-1)/\gamma}\right] \tag{C.2.3}$$

The change in total temperature ΔT_{0s} of equation C.2.3 is defined as shown in equation C.2.4.

$$\Delta T_{0s} = 8.71 \left(\frac{U}{100}\right) \left(\frac{c_a}{100}\right) (\tan\beta_2 + \tan\beta_3) \tag{C.2.4}$$

Using the pressure ratio calculated with equation C.2.3, the total pressure at the outlet of the turbine is calculated. Assuming that the absolute velocity at the inlet is equal to the absolute velocity at the outlet ($c_1 = c_3$) allows the calculation of the static pressure at the turbine outlet (Saravanamuttoo *et al.*, 2001). Equation C.2.5 is used to calculate the static pressure at the rotor inlet (p_2) (Saravanamuttoo *et al.*, 2001).

$$\frac{p_{01}}{p_2} = \left(\frac{T_{01}}{T_2'}\right)^{\gamma/(\gamma-1)} \tag{C.2.5}$$

The respective total pressures are multiplied by the corresponding areas to determine the forces acting on either side of the turbine rotor. It is important to reiterate that the area on the front of the rotor accounts for the effect of the shaft, while the area on the back of the turbine ignores this. How the rotor attaches to the shaft influenced this decision.

With the new compressor and its increased outlet pressure, the force on the front of the turbine is calculated to be equal to 1 506 N. The force on the back of the turbine is 1 374 N. For the old compressor these values are 873 N and 796 N respectively. Hence the load exerted on the shaft with the new compressor installed upstream is 132 N. Without a modified compressor the force is 76 N.

The turbine's contributions to the total axial force are subtracted from those produced by the impeller to determine the resultant force as seen by the bearing. It has increased from 376 N to 955 N. An increase by a factor of 2.54 shows the effect of the pressure ratio increase seen by the impeller.

C.3 Pressure Ratio at Operating Point

Calculations of pressure through the turbine in section C.2 assume an unchanged pressure ration for the turbine. If a solar receiver were installed to absorb the heightened compressor outlet pressure this would hold true. A such, section C.2 represents loading conditions as seen in the final application of the project. For preliminary testing, however, it is more informative to know the increased pressure ratio seen by the turbine.

To determine this the experimental loading curve given by Zhang (2016) was approximated with a second order polynomial. This line was extended to intersect with the new compressor's performance curve (Figure C.2). The pressure ratio at which the the turbine would operate provided that no pressure reducing device is installed between the compressor and the combustor is 2.85.

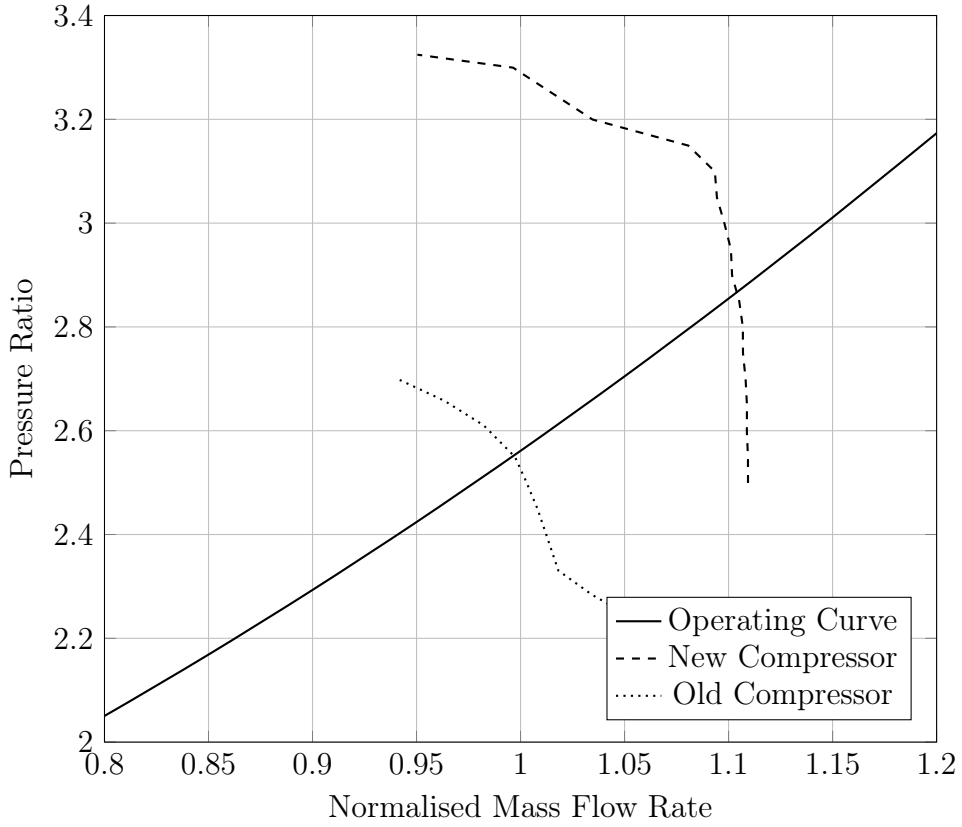

Figure C.2: Operating Curve (adapted from Zhang (2016)) and Compressor Curves (Luiten, 2015)

At a pressure ratio of 2.85 the turbine experiences 231 N on the front and 1 275 N on the back. The total force on the bearing is reduced to 856 N.

Appendix D

Bearing Life Calculation

The exact bearing used in the Rover 1S/60 is not known. Hence its design life calculation done here uses data for a generic angular contact bearing (Budynas and Nisbett, 2015).

An equivalent catalog load rating needs to be calculated. This is then compared to the manufacturer's load rating and if the calculated load rating falls short of the manufacturer's load rating the bearing is fit for service. Limiting this condition are the parameters used to calculated the load rating. Equation D.0.1 shows how to calculate the load rating.

$$C_{10} = a_f F_D \left[\frac{x_D}{x_0 + (\theta - x_0) \left[\ln \left(1/R_D \right) \right]^{1/b}} \right]^{1/a} \tag{D.0.1}$$

The application factor, a_f, in equation D.0.1 serves as a safety factor. It accounts for dynamic effects, overload and general uncertainty. For a device with commercial gearing it is recommended that this factor be set to a value between 1.1 and 1.3 (Budynas and Nisbett, 2015). For the current calculation a factor of 1.2 is used. The Rover 1S/60 was designed for commercial, high technology applications and hence such an application factor is representative of its gearing.

The three Weibull parameters, x_0, θ and b are provided by the manufacturer of the bearing. For the generic bearing used for the present calculation they are 0.02, 4.459 and 1.483 respectively.

From tests of various kinds of bearings, a is determined. For ball bearings it has a value of 3. For both cylindrical and tapered roller bearings it is 10/3.

R_D is the desired reliability of the bearing. Manufacturers usually cal-

culated bearing life with a reliability of 0.9. The current calculation uses a reliability of 0.99 instead.

The force acting on the bearing is F_D. For an angular contact bearing this is a weighted sum of axial and radial forces ($F_D = F_e = X_i V F_r + Y_i F_a$). Weights X_i and Y_i are interpolated from a table that uses F_a/C_0 as the determining column (Budynas and Nisbett, 2015). C_0 is the rated maximum static load of the bearing while C_{10} is the rated design life.

The factor of design life over rated life is represented by x_D. The design life in turn is the product of the design rotational speed and the expected life. The expected life is of interested to the present study. Subsequently equation D.0.1 is rearranged to solve for this value instead. Under the conditions described above the expected life of the bearings is 110 hours.

Appendix E

Drawings

In Figures E.1 to E.4 outer dimensions of the impeller and diffuser are shown. Dimensions of both the design and the final part are shown. Such a comparison is important to quantify the quality of the final product.

Figure E.5 shows the support ring which help the impeller during static deflection testing.

All dimensions shown in this appendix are in millimetre (mm).

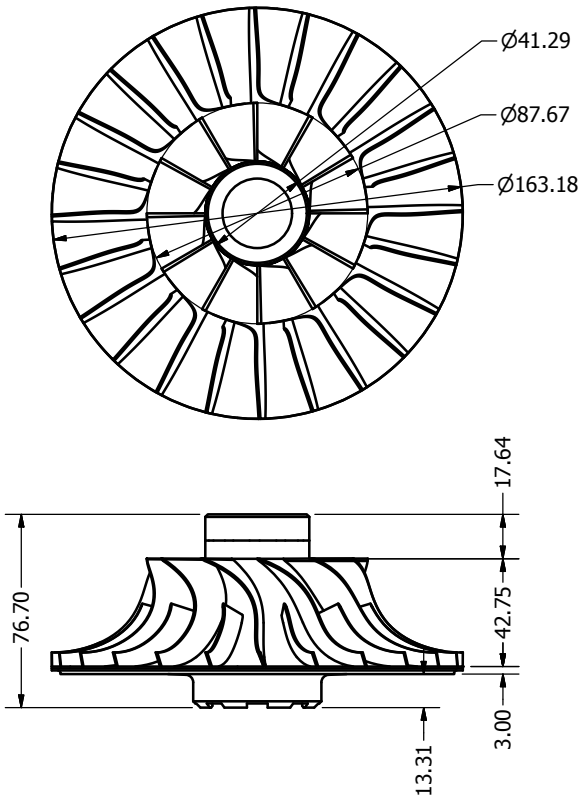

Figure E.1: Impeller Dimensions as Designed

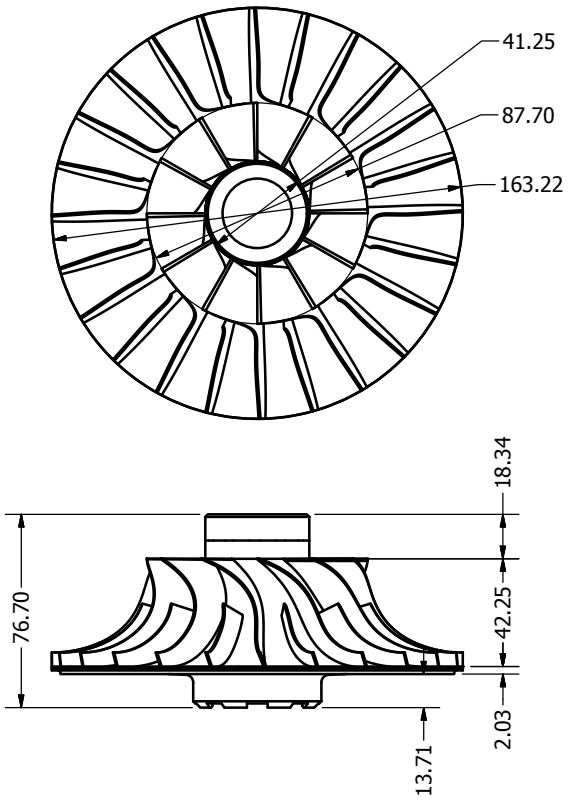

Figure E.2: Impeller Dimensions as Manufactured

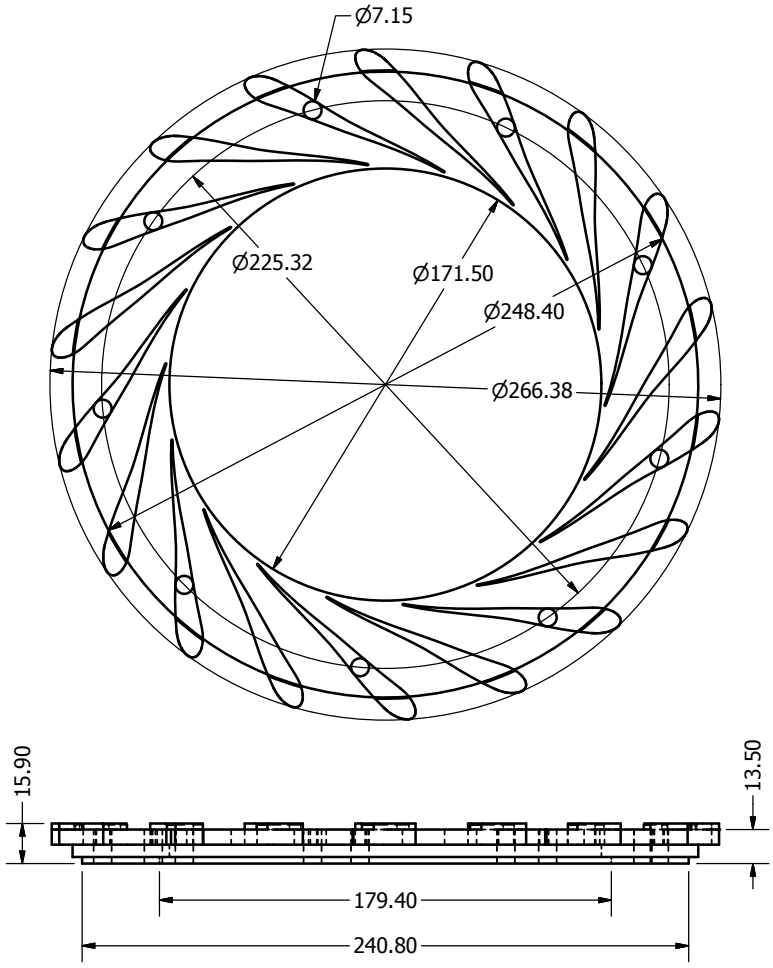

Figure E.3: Diffuser Dimensions as Designed

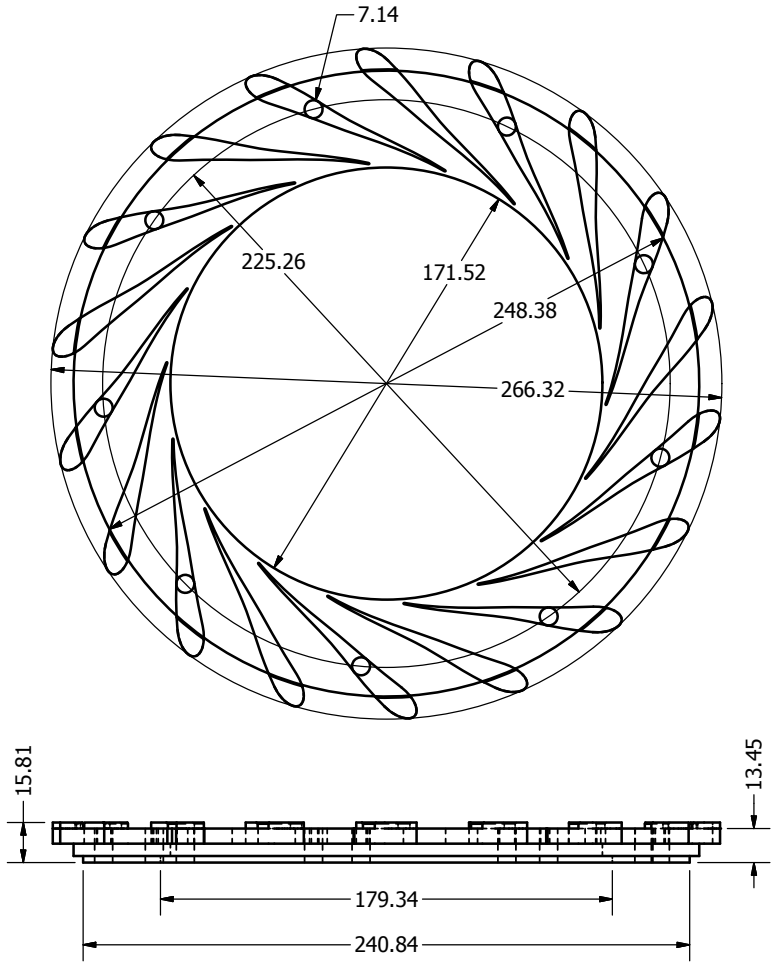

Figure E.4: Diffuser Dimensions as Manufactured

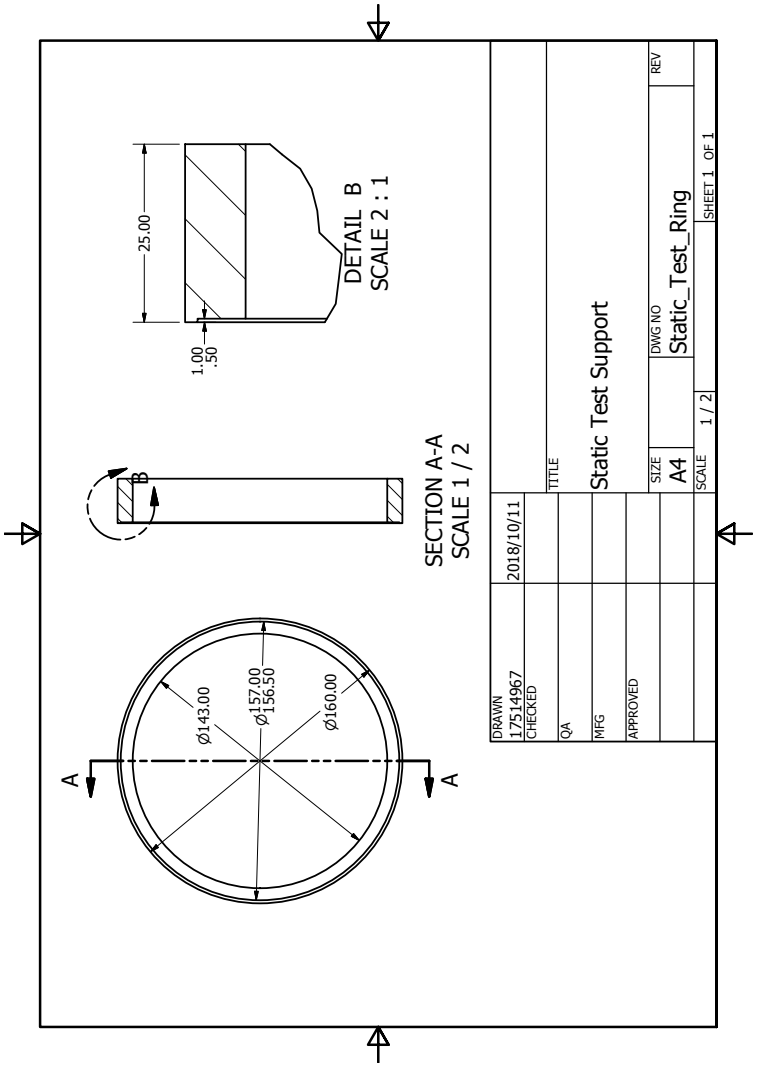

Figure E.5: Dimensions of the Support Ring

Appendix F

Installation of New Components

The impeller is attached to the shaft by means of an interference fit. Once the turbine has been dismantled and the rotor and rotating guide vane unit have been removed from the shaft check the shaft (see (Rover Gas Turbines Limited, 1965) pg. 44). Use tool 33/3001 and check the following:

1. Check that the face most downstream face of the the shaft does not have swash in excess of 0.005 mm.
2. Check run-out of the rotor locating faces. This must not exceed 0.005 mm.
3. Check the high speed pinion does not have run out in excess of 0.013 mm

Once the shaft has been checked, the impeller can be pressed onto it. It is recommended that two tool jigs be manufactured for this and used as shown in figure F.1

1. Degrease the shaft and the impeller.
2. Cool the shaft to -20°C.
3. Fit the alignment tool to the mounting protrusion of the impeller. Align the slots with those in the impeller and tighten the locating screws finger tight only.
4. Place the impeller and mounting tool in a muffle furnace to reach a temperature between 150°C and 200°C.
5. Place the supporting block in the same furnace.

   CAUTION: DUE TO RAPID TEMPERATURE CHANGES IN THE COMPONENTS THE FOLLOWING OPERATIONS MUST BE PERFORMED WITHOUT DELAY.

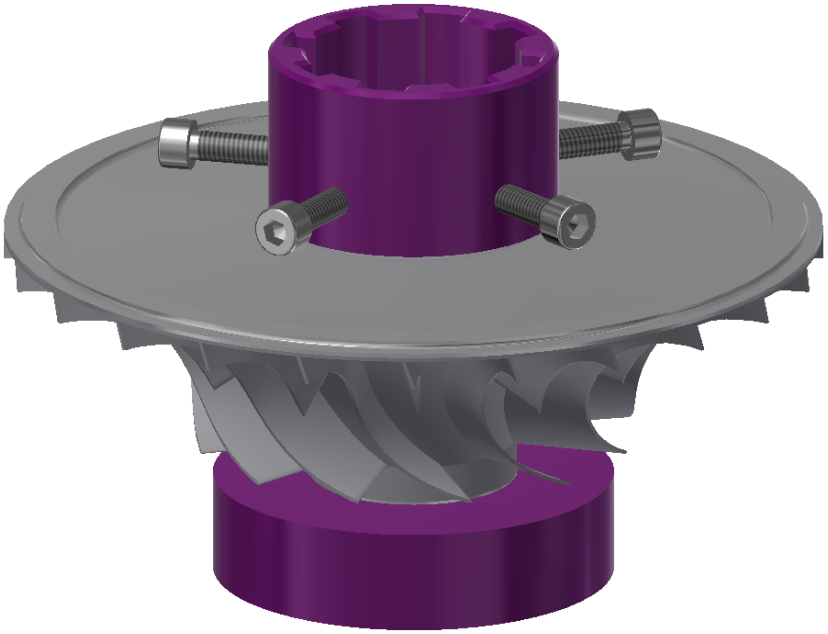

Figure F.1: Alignment Tool and Support Block Relative to Impeller

6. Position the supporting block under the press.
7. Position the impeller and mounting tool assembly in the supporting block under the press.
8. Remove the shaft from the refrigerator and position it in the impeller using the splines of the mounting tool to align it axially.
9. Place a soft metal blank over the end of the shaft. Then lower the ram of the press and leave under two tons of dial load for 3 minutes.
10. Lift the assembly from the press and once it has cooled remove the mounting tool.

F.1 Quality Control

After installation of the new impeller it is important that a swash test be performed to ensure that it is not distorted. It is also important that the impeller be perpendicular to the shaft axis. Use tool 33/3001 (Rover Gas Turbines Limited, 1965) and perform the following steps:

1. Place shaft in the tool. It is recommended that the front end be supported by a 10 mm diameter steel ball. This ball bearing is to be inserted between the shaft and the tool end post.

2. Ensure that the compressor shaft is parallel to the tool's base.

3. Using a stand mounted dial test indicator, check that the rotor swash of the inlet shroud diameter and the disk outer diameter is not more than 0.10 mm.

Appendix G

Velocity Streamlines

Shown below are velocity streamlines calculated with different turbulence models as the pressure ratio increases from 2.1 to 3.3. For these pressure ratios, streamlines in the fine mesh are shown for reference. It is interesting to observe how the large vortex on the low pressure side of the main blade is flattened and then shortened as operating conditions are approached. Note too that this vortex is likely a product of the mesh resolution. For the comparison of turbulence models the coarse mesh is still sufficient.

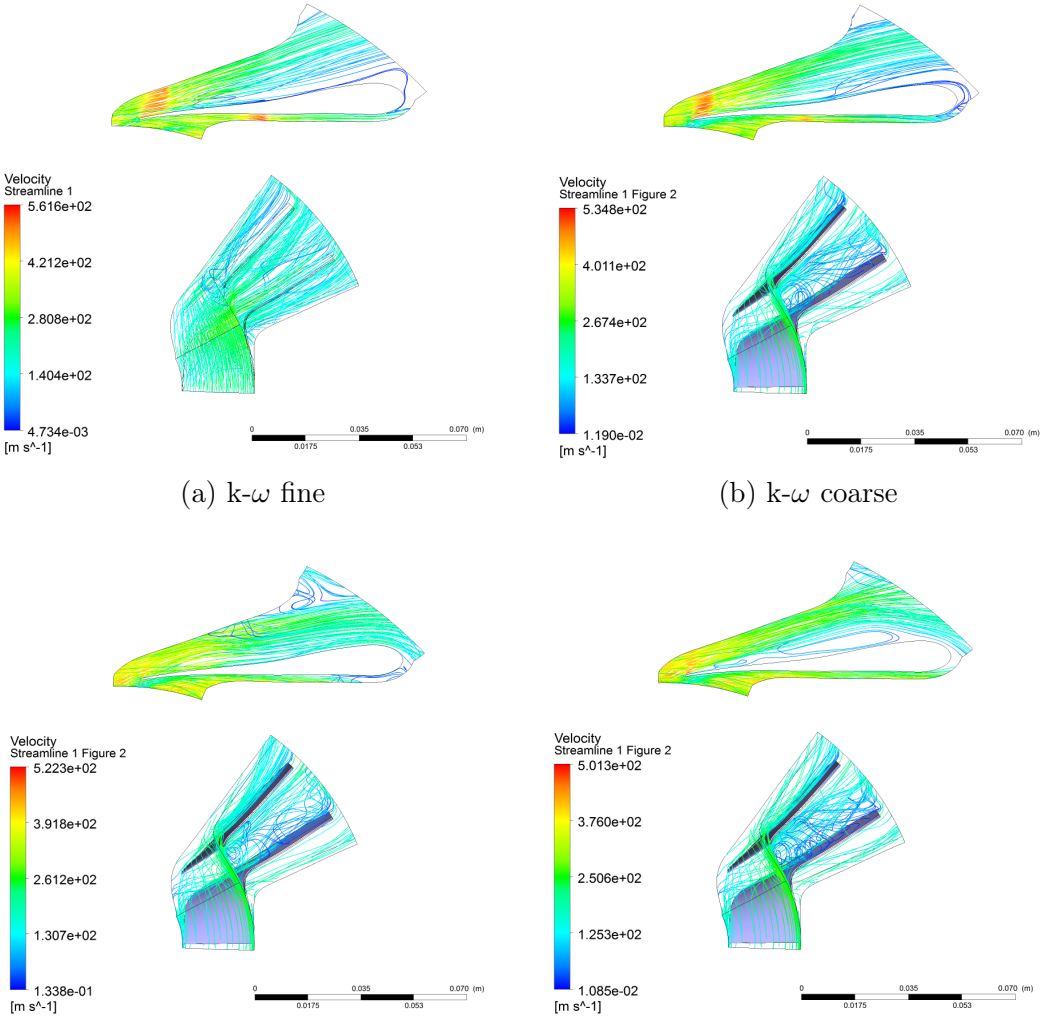

(a) k-ω fine (b) k-ω coarse

(c) k-ω SST (d) SA

Figure G.1: Velocity Streamlines for a Pressure Ratio of 2.7

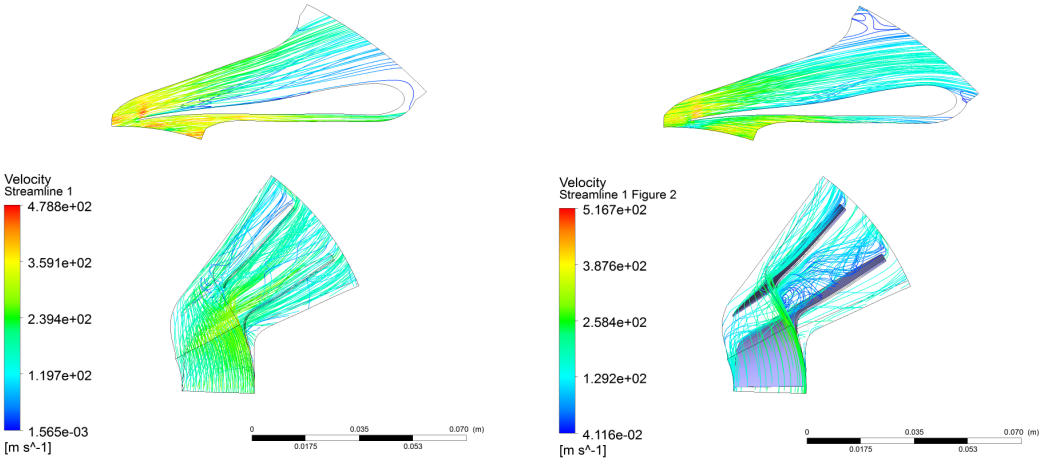

(a) k-ω fine (b) k-ω coarse

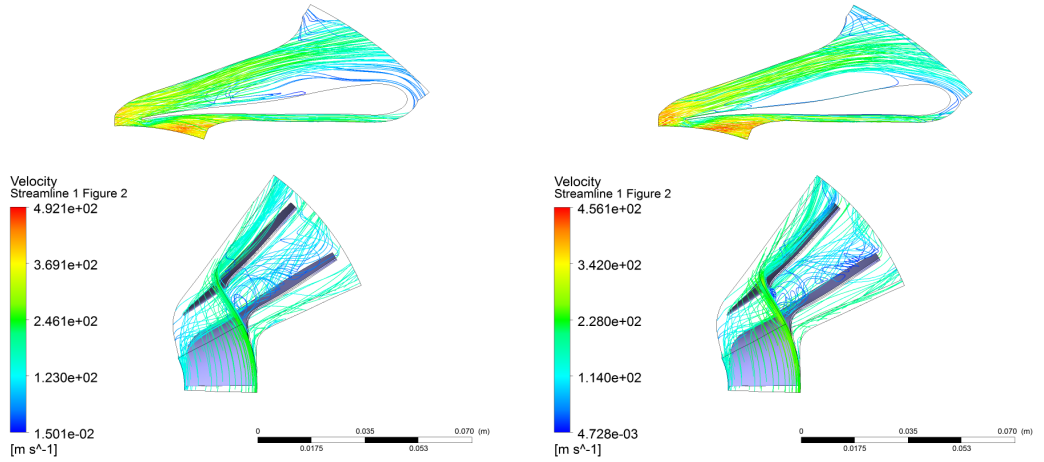

(c) k-ω SST (d) SA

Figure G.2: Velocity Streamlines for a Pressure Ratio of 3.0

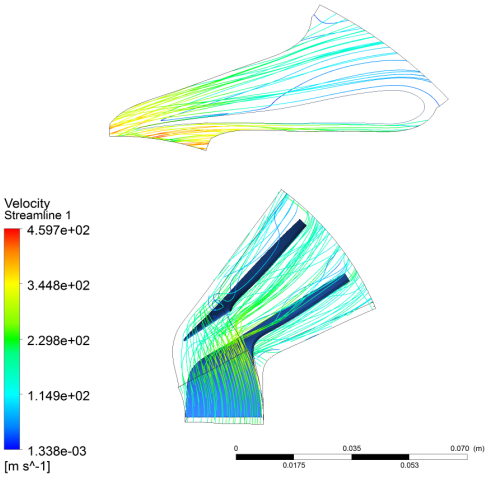

(a) k-ω fine

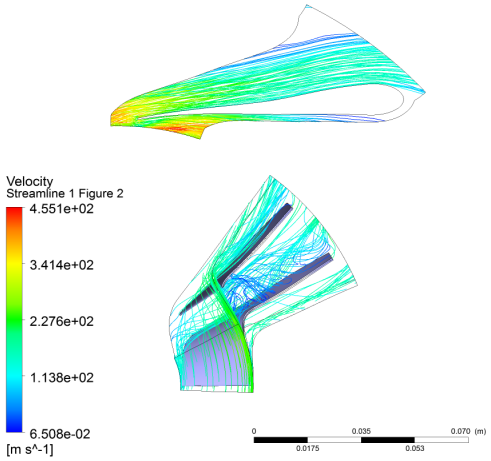

(b) k-ω coarse

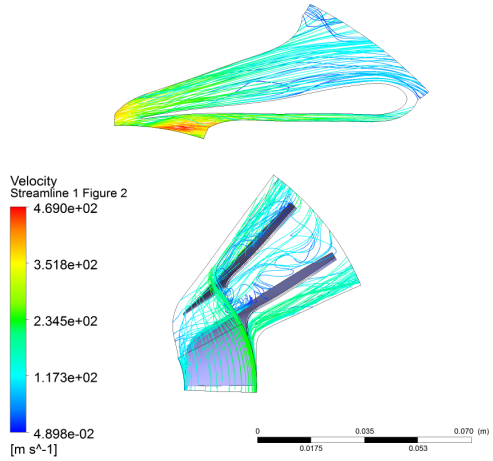

(c) k-ω SST

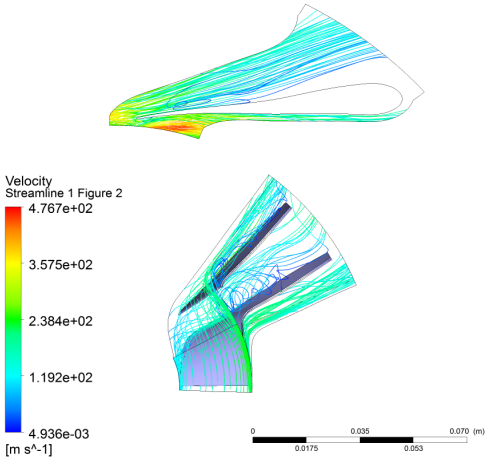

(d) SA

Figure G.3: Velocity Streamlines for a Pressure Ratio of 3.2

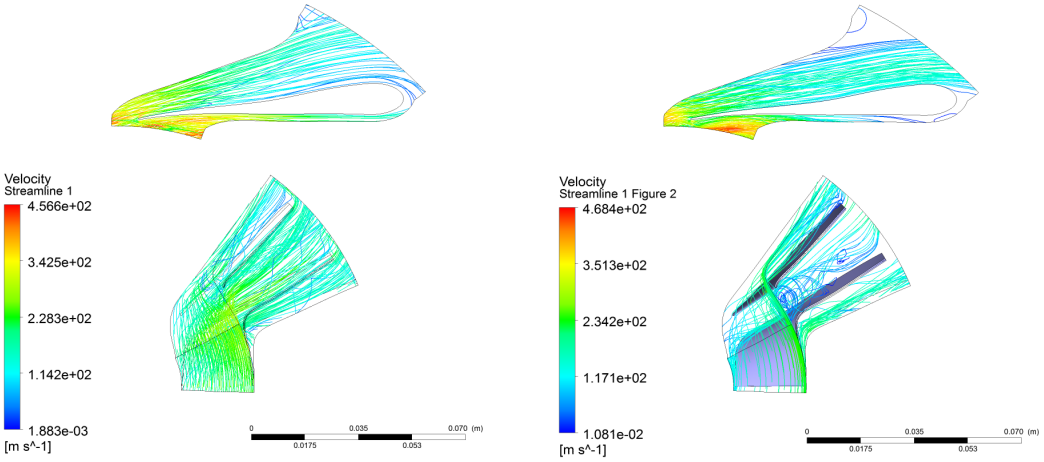

(a) k-ω fine (b) k-ω coarse

Figure G.4: Velocity Streamlines for a Pressure Ratio of 3.3